Fracture in Living Cell Monolayers

Julia Duque[1,*], Alessandra Bonfanti[2], Jonathan Fouchard[1,#],
Emma Ferber[1], Andrew Harris[1,+], Alexandre J. Kabla[3,*], Guillaume T. Charras[1,4,5,*]

[1] London Centre for Nanotechnology, University College London, London, UK
[2] Department of Civil and Environmental Engineering, Politecnico di Milano, Milan, 20133, Italy
[3] Department of Engineering, University of Cambridge, Cambridge, UK
[4] Institute for the Physics of Living Systems, University College London, London, UK
[5] Department of Cell and Developmental Biology, University College London, London, UK
[#] Current address: Laboratoire de Biologie du Développement (LBD), UMR 7622 CNRS - Sorbonne Université, INSERM ERL U1156, Institut Biologie Paris Seine (IBPS)
[+] Current address: Mechanical and Aerospace Engineering, 1125 Colonel By Drive, Ottawa, Ontario, Canada K1S 5B6

[*]To whom correspondence may be addressed: j.duque@ucl.ac.uk, ajk61@cam.ac.uk, g.charras@ucl.ac.uk.

Abstract

The ability of tissues to sustain mechanical stress and avoid fracture is a fundamental pillar of their function. Fracture in response to physiological levels of stress can be undesired, for example resulting from disease or genetic mutations, or be an integral part of developmental processes, such as during blastocoel formation in mouse or during leg eversion in flies. Despite its importance, we know very little about fracture in cellularised tissues because it is a multi-scale process that necessitates comprehension of the interplay between mechanical forces and processes at the molecular and cellular scales. Using a combination of mechanical measurements, live imaging and computational modelling, we characterise fracture in epithelial monolayers. We show that, despite consisting of only a single layer of cells, monolayers can withstand surprisingly large deformations, often accommodating several-fold increases in their length before rupture. To protect against large deformation, epithelia increase their stiffness multiple-fold in a process controlled by keratin intermediate filaments. Perturbing keratin organisation fragilised monolayers and prevented strain stiffening. Using computational approaches, we show that, although the kinetics of bond rupture ultimately control fracture, tissue rheology and the history of deformation prior to failure set the strain and stress that the tissue reaches at the onset of fracture. Our data paint a picture of epithelia as versatile materials that combine resistance to shocks with deformability when subjected to low strain rates.

Introduction

During development and normal physiological function in adult tissues, epithelial monolayers withstand mechanical stresses that differ markedly. In embryonic morphogenesis, tissues undergo large deformations over periods of hours or days. For example, convergence and extension in *Xenopus Laevis* typically leads to a 3 - 4 fold increase in tissue length over a span of ten hours, a process enabled by rearrangement of adhesive contacts at the cellular-scale. In contrast, deformations in adult tissues are typically smaller and take place on shorter time scales with fixed tissue organisation. For example, the myocardium tissue deforms by 10 - 20% in 200 ms [1], lung alveoli deform by $\sim$ 20% up 20 times a minute during breathing [2], and the skin deforms by over 50% in fractions of a second during limb movement [3], [4]. The mechanical role of epithelia is particularly apparent in disease. Mutations in intermediate filaments and desmosomal proteins in the epidermis lead to epidermolysis bullosa, a family of diseases characterised by fragile skin that fractures in response to physiological levels of deformation [5], [6]. Despite its importance, we know relatively little about the strength of epithelia and the biological structures that control it, partly because of the difficulty of characterising fracture in cellularised tissues.

Fracture is a permanent break of a material into smaller components when subjected to stress. Loss of material integrity can occur once a threshold of strain or stress is exceeded and the mode of fracture often depends on the rate of stress application. While much is known about fracture in classic engineering materials such as ceramics and steel [7, 8], fracture in soft materials is still an active research field [9, 10, 11]. Tissue fracture is inherently a multi-scale process with deformations applied at the tissue-scale resulting in stress at the cellular-scale that causes rupture of intercellular adhesion complexes at the molecular-scale. Further complexity arises because of the viscoelastic properties of living tissues that stem from biological processes with distinct time-scales, such as protein turnover occurring over tens of seconds to tens of minutes, cell intercalation over tens of minutes to hours, and upregulation of cell division taking hours. Thus, fracture in living tissues involves processes spanning multiple length- and time-scales.

Fracture can occur either in response to extrinsically applied forces or in response to forces generated by the cells within a tissue. While we are familiar with the former from our everyday experience, the latter is unique to living tissues and is a normal part of some developmental processes. Indeed, tissues can self-rupture as a consequence of local upregulation of active stress due to myosin contractility, motility on a substrate, or an increase in osmotic forces to ensure the proper development of embryonic structures. For example, during eversion of the *Drosophila* leg, the squamous peripodial epithelium first delaminates from its collagenous substrate before rupturing in response to a local increase in cellular contractility [12]. *Trichoplax adhaerens*, a flat marine metazoan, reproduces asexually by fissions induced by movement of different parts of its body in opposite directions[13]. During blastocoel formation in the mouse, cracks occur between the inner mass cells in response to osmotic pumping [14], [15]. In gastrulation, tissue integrity is transiently lost because of an epithelial to mesenchymal transition (EMT) that is thought to involve an upregulation in cell contractility [16]. Excess intrinsic stresses can also result in unwanted rupture. For example, depletion of myosin phosphatase leads to excessive contractility in the *Drosophila* amnioserosa, giving rise to frequent breaks between cells [17]. At the onset of metastasis, tumour

cells undergo EMT in a process dependent on myosin contractility [18]. Collectively, these phenomena suggest that tissues have the intrinsic ability to self-rupture. However, it remains unclear if fracture in response to extrinsic and intrinsic forces occurs through the same biophysical processes.

Here, by using suspended epithelial monolayers of MDCK cells, we investigate fracture at the tissue-scale by subjecting tissues to ramps in deformation. We also show that fractures occurring in response to increases in contractility are mechanically similar to fractures due to externally applied deformation. At high deformation, we reveal that epithelia strain-stiffen to limit the amount of deformation they undergo. Surprisingly, actomyosin is not the main contributor to mechanics at large deformation, rather this is dominated by a supracellular network of keratin filaments. Finally, using computational modelling, we link strain at the tissue level to rupture of intercellular adhesion bonds at the molecular scale to predict the onset of fracture. We show that tissue-scale rheology interplays with molecular bond rupture kinetics to govern tissue fracture.

Results

Epithelial monolayers can withstand large deformations before rupture

To investigate the response of living tissues to externally applied deformation, we used Madin-Darby canine kidney (MDCK) monolayers devoid of a substrate and suspended between two test rods [19]. In these conditions, all of the force applied to the monolayer is borne by intercellular junctions and transmitted through the cytoskeleton (**Fig. 1a**), making this an ideal system to explore the operating limits of a living cellularised material.

After preconditioning (materials and methods), we subjected monolayers to a ramp in deformation applied at a constant strain rate of 1% s^{-1} (**Fig. 1b** , **Movie S1**) to minimise stress originating from viscoelastic contributions [20], and we monitored stress as a function of time. Monolayers could withstand more than a 3-fold increase in length before the first cracks appeared and failed for strains of $\sim$ 300% (**Fig. 1c**). Cracks first appeared at either of the free edges before propagating through the material until failure (**Fig. 1d**). As the monolayer length ($\sim$ 3mm) is several orders of magnitude larger than its thickness ($\sim$ 10 μm), we approximated the tissue to a thin sheet and normalised the force F to the width w_0 of the monolayer prior to deformation to generate tension-strain curves. In response to deformation, tension first rose linearly up to $\sim$ 50% strain before increasing more rapidly until reaching a peak tension $\Gamma^* = F^*/w_0$ (**Fig. 1c**). Beyond this strain, cracks became apparent and tension decreased until complete rupture of the monolayer. In many materials, the peak tension corresponds to the onset of fracture. Therefore, we plotted the strain ε^* at which Γ^* was reached as a function of the strain $\varepsilon_{1^{\text{st}}\text{defects}}$ at which we visually observed the first monolayer defects in our time-lapse images (**Fig. 1d**). This revealed a clear correlation (**Fig. 1e**), suggesting that crack initiation results from accumulated stress in the tissue. In the following, we used Γ^* and ε^* as parameters to characterise the onset of fracture in epithelial monolayers.

In classic engineering materials, ruptures occur when stress reaches a threshold tension. To determine whether crack propagation resulted from maintenance of such a threshold, we plotted the force F normalised by the width of the monolayer at each time $w(t)$ (**Fig. 1f**-(i), see methods). This revealed the presence of a plateau in tension after the appearance of the first defect that persisted as fracture propagated through the material (**Fig. 1f**-(ii), red curve). This indicated that epithelial monolayers break after reaching a tension threshold Γ^* that remains approximately constant throughout the process of rupture.

Cracks occur at cell-cell junctions

After characterising fracture at the tissue-scale, we examined the phenomenon at the cell-scale. Cracks could in principle appear either because of cell lysis or rupture at intercellular junctions. High magnification phase contrast imaging revealed that cells were very elongated at the free edge of the monolayer where cracks initiate (**Fig. 1h**). As strain increased, cell-cell contacts appeared to progressively decrease in size perpendicular to the direction of applied stretch before the cells lost contact with one another. The crack front alternated phases of rapid growth and pauses with no apparent preferred directionality. In all cases, it followed cell-cell junctions and cells appeared

to peel apart from one another at intercellular contacts. When we examined the localisation of E-cadherin (a key component of adherens junctions), we noticed disappearance of the cadherin signal from the cell surface after a cell-cell junction had separated (**Fig. S1c**, **Movie S2**). In cross-sectional views we observed a progressive decrease in the height of adherens junctions as strain increased with no significant change in the average fluorescence intensity of E-cadherin (**Fig. 1g, Fig. S1d, e**). This suggests that intercellular junction rupture first involves a decrease in junction height due to progressive breakage of intercellular bonds in response to stress, before catastrophic failure occurs once the junction has thinned sufficiently and a critical number of bonds has been lost.

Epithelial monolayers can self-rupture by increasing their contractility

In vivo, epithelia can rupture in response to an increase in contractility. In some cases, this gives rise to defects that will impair the viability of the organism, while in others it forms part of the normal developmental program. For example, in the *Drosophila* amnioserosa, depletion of the myosin phosphatase MBS gives rise to small localised tears in the tissue disrupting the next developmental state [17]. Conversely, during eversion of the *Drosophila* leg [12], the peripodial membrane must irreversibly rupture to allow correct development of the leg. To better understand the response of tissues to active stresses generated by myosins, we examined the response of epithelia to calyculin, a myosin phosphatase inhibitor that increases monolayer tension [21].

In our experiments, we incubated monolayers with 20 nM calyculin and monitored their response in tension while imaging their morphology (**Fig. 2a, Movie S3**). Monolayers were unperturbed until $\sim$ 90 minutes after the addition of calyculin, when holes appeared in the epithelium (**Fig. 2b, e**). These holes grew in time, merging together and eventually causing full rupture of the monolayer (**Fig. 2e**). As in ramp experiments, cracking occurred at intercellular junctions (**Fig. 2b**). Although E-cadherin was lost from the cell surfaces whose intercellular junctions had ruptured (**Fig. 2b**), we did not notice any systematic loss of E-cadherin preceding crack formation. In contrast to ramp experiments, cracks mostly formed in the bulk of the tissue rather than at the edges (**Fig. 2e**). From the onset of treatment, tension gradually rose in the monolayer reaching a peak after $\sim$ 90 minutes before decreasing until tissue rupture (**Fig. 2c**). As in ramp experiments, when we computed the tension taking into account the evolution of monolayer width (**Fig. 2d**-(i)), we found that tension reached a maximum at the onset of rupture and remained constant as cracking progressed, reinforcing the idea of a threshold tension necessary for fracture (**Fig. 2d**-(ii), red curve). Similar to the ramp experiments, the time $t_{1^{st}defects}$ at which the first defects were observed was correlated with the time t^* at which tissue tension reached a maximum, further confirming Γ^* and t^* as good criteria for rupture onset (**Fig. 2f**). Intriguingly, tension at rupture was $\sim$ 10 - fold lower than for ramps and the rupture time $\sim$ 10 times longer.

Given that calyculin is a broad spectrum phosphatase inhibitor, we confirmed that the monolayer rupture and the increase in tension that we observe are specific to cell contractility. First, using immunostaining, we verified that calyculin increased myosin phosphorylation and promoted the formation of stress fibers but did not appear to perturb E-cadherin or cytokeratins over durations for which we typically observed changes in the mechanics of the monolayers (**Fig. S2g - i**). Next,

we incubated the monolayers with a specific myosin inhibitor, blebbistatin, for 30 - 40 min prior to calyculin addition (**Fig. 2g, Movie S4**). This ensured that any effect of calyculin specific to myosin contractility was inhibited. When only blebbistatin was present, tension decreased, as expected [21] (**Fig. 2h**, blue shaded area). After calyculin addition, the tension remained low and monolayers did not rupture over durations that typically led to failure when using calyculin treatment alone (**Fig. 2h, Fig. S2c, d, Movie S5**). Altogether, we concluded that increasing contractility in suspended epithelial monolayers is sufficient to generate rupture.

Rupture strain, tension, and time scale with strain rate

During normal physiological function, cells in some adult tissues can experience deformations of hundreds of percent at strain rates ranging up to 100% s^{-1}, while others experience far slower loading [1]. To explore this while minimising viscous contributions, we examined crack formation in monolayers subjected to ramps in deformation for a range of strain rates (0.1 - 3% s^{-1}).

For each monolayer, we characterised the rupture tension Γ^*, the rupture strain ε^*, and the time t^* at which Γ^* was reached. When we plotted our data as a function of strain rate, we found that Γ^* increased with strain rate, from 0.04 Nm^{-1} at 0.1% s^{-1} until seemingly reaching a plateau of $\sim$ 0.20 Nm^{-1} for strain rates above 2% s^{-1} (**Fig. 3a**). In contrast, both ε^* and t^* decreased with increasing strain rate. Rupture strains decreased from $\sim$ 700% at 0.1% s^{-1} until reaching a plateau of $\sim$ 300% for the larger strain rates, comparable to those observed in *T. adhaerens* which deforms at 20% s^{-1} [13] (**Fig. 3b**). Rupture time t^* spanned two orders of magnitude decreasing from 10^4 to 10^2 s (**Fig. 3c**). As previous work has shown that no cell rearrangements and only few cell divisions take place over hour-long periods in our suspended monolayers [22], these large deformations are likely accommodated through remodelling of the cytoskeleton. Interestingly, for the lowest strain rate 0.1% s^{-1}, rupture tension Γ^* and time t^* were comparable to those observed in response to calyculin treatment, suggesting that rupture due to active stresses generated by myosin contractility and passive stresses due to deformation of the cytoskeleton may arise from the same biophysical processes.

To gain insight into the failure mechanism of the material, we plotted the rupture tension as a function of the rupture time and rupture strain. This revealed that rupture tension Γ^* scaled as $\sim \log(1/t^*)$ (**Fig. 3d**), reminiscent of the failure dynamics of groups of microscopic bonds subjected to force [23, 24]. Experiments increasing contractility clustered with experimental data from ramps (**Fig. 4a**), further suggesting that the actual origin of stress may not be important in this process. Rupture tension decreased linearly with rupture strain (**Fig. 3e**) and, as a consequence, the strain energy at rupture onset remained approximately constant across strain rates (**Fig. S3g**). This behaviour is surprising because, contrary to our everyday intuition handling elastic materials, larger rupture tensions are associated with smaller rupture strains in epithelia (**Fig. 3e**).

Monolayers display a strain rate-dependent strain stiffening

One potential origin for this counter-intuitive behaviour could involve a change in the mechanical response of the monolayer as strain rate changes. In monolayers stretched at 1% s^{-1}, the slope of

the tension-strain curve visibly increased for strains larger than $\sim 50\%$ (**Fig. 1c**). This feature, known as strain-stiffening (**Fig. 3f**), has also been observed in biopolymer networks, providing them with greater ability to limit deformation and resist fracture [25]. Therefore, we characterised strain stiffening further and examined how it changed with strain rate. When we computed the gradient of the tension-strain curve for monolayers subjected to ramps at strain rates of 1% s^{-1}, we observed three distinct regimes: first, until $\sim 30\%$ strain, the gradient was constant; then, between $\sim 50\%$ and 100% it increased monotonically with strain, and finally from around 100% strain, it reached a maximum value (**Fig. 3g**). The gradient in the third regime was $\sim$ 6-fold larger than that in the first (**Fig. 3h**). Intriguingly, monolayer strain-stiffening was dependent on strain rate (**Fig. 3i**). At the lowest strain rate (0.1% s^{-1}), no change in the tension gradient at high strain was apparent but, from 0.3% s^{-1}, the magnitude of stiffening increased with strain rate, saturating for rates above 2% s^{-1}, a behaviour known as shear stiffening (**Fig. S3e, f**).

Strain stiffening might arise from mechanotransductory processes or from the intrinsic organisation of the cytoskeleton and cells within monolayers. We noticed stiffening for strain rates above 0.3% s^{-1} with the most pronounced observed for 3% s^{-1}, signifying that a hypothetical mechanotransductory process should take place over durations shorter than ~ 300 seconds. This points to adaptive processes involving post-translational modifications or protein recruitment downstream of detection rather than transcriptional changes. Therefore, we examined known mechanisms such as recruitment of vinculin downstream of the unfolding of alpha-catenin [26], [27], as well as EPLIN [28] and E-cadherin recruitment induced by tension [29]. For this, we generated monolayers expressing each of these proteins tagged with GFP and subjected them to strains of 30 - 80% for 30 minutes. However, we could not observe recruitment of any of these proteins (**Fig. S7**). This suggested that strain stiffening is more likely to arise from the intrinsic organisation of the cytoskeleton in monolayers.

As strain stiffening may act as a protective mechanism against fracture and because we observe the same trend to saturation in stiffening and rupture tension, we decided to investigate the origin of this effect and its role in governing the strength of epithelial tissues.

Strain-stiffening and fracture are independent of actomyosin

Actomyosin is arguably the main determinant of cell shape and a key player in cell mechanics. In tissues, the actomyosin cortex controls monolayer rheology at low strain (around 30 - 50%) before strain stiffening is observed [20], [21]. Therefore, we examined the role of myosin contractility and F-actin in strain stiffening by repeating our ramp deformation experiments at 1% s^{-1} for monolayers in which myosin contractility had been inhibited or enhanced and monolayers were actin polymerization had been inhibited (**Fig. 4b**). For this, we blocked myosin activity with blebbistatin and we increased phospho-myosin levels by treating monolayers with calyculin for 20 minutes, a duration sufficient to increase pre-tension but not to cause rupture (**Fig. 2c, Movies S6, S8**). Neither treatment affected strain stiffening (**Fig. 4b**). Next, to examine the role of F-actin, we treated monolayers with latrunculin, an inhibitor of actin polymerisation that leads to global loss of F-actin (**Fig. 4e, Movie S9**). Similar to myosin, F-actin appeared to play no role in strain-stiffening (**Fig. 4b**). Interestingly, none of these treatments affected the rupture

characteristics of monolayers (**Fig. 4c - e, S4a - c**). Hence, the mechanics of epithelia at high strain appears independent of actomyosin.

Keratin filaments control monolayer strength

We then focused our attention on keratin intermediate filaments. These form entangled networks in the vicinity of the nucleus with wavy filament bundles radiating out towards the cell membrane where they connect to neighbouring cells via specialised complexes. These intercellular adhesion complexes, known as desmosomes, comprise desmosomal cadherins whose extracellular domains bind to counterparts on other cells while their cytoplasmic domains connect to keratin filaments via proteins such as desmoplakin and plakoglobin [30]. Keratins can extend to multiple times their original length before rupture and can bear high tensile load, making them good candidates to maintain tissue integrity at high deformation [31, 32, 33, 34]. Previous work has highlighted a mechanical role for desmosomes and shown that, as cells are stretched, desmosomes become progressively loaded [35]. Keratins and desmosomes have also received much interest from a clinical point of view for their role in the maintenance of skin integrity. Mutations in Keratins and desmosomal proteins give rise to skin blistering disorders with symptoms of mechanical fragility [36], [5]. Thus, the supracellular network formed by keratins and desmosomes appears as a promising structure to contribute to tissue mechanics.

We first imaged the keratin filament network conformation in response to stretch by imaging monolayers stably expressing K18-GFP at high magnification. At low strain, keratin bundles extending towards the cell periphery had wavy morphologies, similar to those observed on glass. As strain progressively increased, the network became visibly stretched in the direction of deformation, suggesting that keratin filament bundles become loaded as previously reported [31, 37] (**Fig. 5a**). Even when applying strains larger than 300%, the network retained its structural integrity, although holes did form above 400% strain. To understand the role of keratins and desmosomes, we perturbed each of these structures in turn and assessed their impact on tissue mechanics. To study the contribution of keratins, we overexpressed a dominant mutant of Keratin 14, K14-R125C, which is found in some epidermolysis bullosa patients [36]. Immunostaining against Keratin 18 in K14-R125C monolayers revealed a very aggregated keratin network compared to the extensive supracellular network observed in control monolayers, consistent with previous work [38], [39] (**Fig. 5c**). Although the desmoplakin organisation appeared normal, connections of intermediate filaments to desmosomes were missing. To determine if the connection between cellular keratin networks is important for tissue mechanics and force transmission, we also engineered a cell line with a stable desmoplakin depletion (DSP-shRNA) to perturb desmosomes. We first confirmed that the keratin network of DSP-shRNA cells failed to attach to the membrane (**Fig. 5d** yellow boxes). In addition, keratin networks collapsed around the nucleus instead of displaying their characteristic stellate organisation (**Fig. 5d** arrowheads). We next examined whether the perturbation to the keratin network observed in both K14-R125C and DSP-shRNA monolayers affected tissue mechanical response by performing ramp experiments at 1% s^{-1} (**Fig. 5b, S5a, Movies S1, S10** and **Movies S11, S12**). Visually, we observed that both perturbations led to earlier rupture than in controls (**Fig. 5b, S5a** arrowheads). Quantitatively, both the rupture strain, ε^*, and the rupture tension, Γ^*, were significantly lower in the perturbed tissues (**Fig. 5e-h, S5f-i**). These data confirm that keratin

networks connected across cells are necessary for monolayers to resist large deformations.

Strain stiffening depends on the integrity of a keratin supracellular network

We next investigated the contribution of keratin filament networks to strain-stiffening by computing the tension gradient in K14-R125C and in DSP-shRNA monolayers (**Fig. 6b-, d-**(i)). These presented two main features that differed from controls. First, in both perturbations, there was no increase in the tension gradient with strain in contrast to the stiffening observed in controls (**Fig. 6b-, d-**(ii)). This indicated that both the keratin network and its attachment to cell junctions are necessary for monolayers to strain-stiffen. Second, in the DSP-shRNA monolayers, we detected larger values of the tension gradient at low strains compared to control (**Fig. S5b, d**). Although this was surprising, we reasoned this may arise because of a compensation mechanism as observed by others. For example, when tight junctional proteins ZO1 and ZO2 are depleted [40], cells become more contractile. Further, the expression of a dominant negative of Desmoplakin exposes the α18 epitope in α-catenin leading to adherens junction compaction [41]. To investigate the molecular mechanism underlying the increase in tension gradient, we immunostained DSP-shRNA and control monolayers against phospho-myosin (pMLC), F-actin, and E-cadherin. In DSP-shRNA monolayers, we visually observed a clear increase in pMLC and actin stress fibers as well as E-cadherin (**Fig. S5e** respectively). Therefore, DSP-shRNA monolayers are stiffer at low strains but more fragile at high strains despite having more F-actin, pMLC and E-cadherin (**Fig. S5e**, **Fig. S6g**). When we perturbed actomyosin organisation, we could not observe any impact on strain stiffening (**Fig. 4b**) or the rupture characteristics of monolayers (**Fig. 4c - e**), implying that the structure that controls these properties is not affected by treatment with latrunculin, blebbistatin or calyculin. Therefore, we confirmed by immunostaining that these drugs did not affect the keratin network (**S2i, Fig. S4d**). Our results confirm that strain-stiffening is dependent on the presence of a supracellular keratin network pointing to a key role in governing the response of monolayers at high strains.

Finally, we investigated if intermediate filament perturbation affected the strain rate dependency of strain stiffening, rupture tension and rupture time (**Fig. S6a - c**). For this, we subjected K14-R125C monolayers to ramps at two different strain rates, 1% s^{-1} and 0.3% s^{-1}. Neither rupture tension nor rupture strain changed with strain rate (**Fig. S6a, b**), in contrast to control monolayers. When we plotted these experiments in tension-strain or tension-time plots, we found that they presented a trend very different from the ramp experiments performed on WT monolayers (**Fig. 6e, f**).

In summary, we show that intermediate filaments are primarily responsible for load bearing at high strain and that strain-stiffening also depends on this network. Altogether, our results point to keratin intermediate filaments as the main structure protecting epithelial monolayers against large deformations.

Non-linear rheology and collective dynamics of bond rupture control the onset of fracture in epithelial monolayers

The onset of rupture is associated with the separation of cell junctions. At the molecular level, this implies unstable dynamics with bonds dissociating more frequently than they associate. Simple models of interfaces linked by dynamic bonds have already demonstrated that a molecular slip bond behaviour may lead to a finite time of separation that decreases with the mechanical tension applied to the system [23, 24]. Such a trade-off between time-to-fracture and applied mechanical force is consistent with our observation that monolayers reach higher rupture tension Γ^* and shorter rupture times t^* at large strain rates. However, we also observed that the strain at the onset of fracture decreased with strain rate (**Fig. 3b**): the higher the fracture tension, the lower the strain at rupture (**Fig. 3e**). Remarkably, this qualitative trend is not present when the intermediate filament network is disrupted and the shear-stiffening behaviour of the monolayer is abrogated. Although junction separation is primarily controlled by the tension it is subjected to, this tension results from a multitude of processes, ranging from deformations or forces imposed upon the tissue to active contractile behaviours. Furthermore, the boundary conditions influence the resulting mechanical state of the tissue. The onset of monolayer rupture therefore likely involves the interplay between the tissue-scale monolayer rheology and the molecular-scale dynamics of bonds. We hypothesise here that this interplay is responsible for the range of behaviours reported in this study.

A stochastic slip bond dynamics model inspired by the work of [23] and [24] combined with a range of material models enabled us to explore the qualitative and quantitative agreement of this hypothesis with our data (see methods). In essence, two surfaces representing an intercellular junction are connected by a population of N independent linkers that can exist in two states, bound or unbound. They bind at a fixed rate k_{on}, but unbind at a rate k_{off} that increases exponentially with mechanical load (**Fig. 7a**). In this particular implementation, all bound linkers equally share the tension applied to the surfaces. Fracture is assumed to be triggered when the system transitions to a state where all links detach (**Fig. 7b**). When a constant force is applied to a junction, we find as expected that the larger the applied force is, the shorter the time to rupture (**Fig. 7c**).

In our experiments, the force is not constant but instead results from ramps of deformation applied at different rates. The tension in the tissue for a given strain rate is a function of time that depends on the material's rheology. For a range of strain rates and material models, we can calculate the temporal evolution of the applied tension. The bond dynamics can then be simulated a large number of times in order to get statistics for the rupture parameters Γ^* and t^*. The corresponding value of ε^* is then determined using the rheological model.

To grasp the role of rheology in the fracture behaviour, we considered in the first instance the simple case of a linear elastic relationship between stress and strain. This corresponds to the low strain rate limit identified in [20, 42], for relatively small deformations. As expected, the rupture load increases with strain rate (**Fig. S 9a**), but so does the strain at fracture (**Fig. 7d**); this arises because stress and strain are proportionally related to each other through the constitutive equation of the material. A more complex material model takes into account the rich time-dependent linear rheological behaviour that we previously validated at low deformation [42]. However, even in this

case, the relationship between rupture strain and strain rate remains a monotonically increasing function (**Fig. 7e**).

Our experimental observations show that the material strain-stiffens for strains larger than $\sim 50\%$, but also that stiffening is larger for large strain rates. This shear stiffening behaviour is a classical feature of random fibre networks [43, 44, 45]. The phenomenon can be understood in a number of ways; at a basic level, as strain increases, more and more fibres align along the direction of deformation and become taut, signifying that more fibres are progressively recruited to carry the mechanical load. As a result, the stiffness of the network increases with the number of recruited fibres and hence with applied strain. In our case, intermediate filament bundles appear to be responsible for both strain-stiffening and shear-stiffening. As keratin intermediate filaments do not intrinsically strain-stiffen [34], we hypothesise that progressive recruitment of intermediate filaments to bear load underlies the strain stiffening observed in experiments. To account for this behaviour, we introduce a non-linear elastic model where springs are progressively recruited as the deformation increases, leading to the tension-strain characteristics presented in **Fig. 7f** (see Methods). This implementation displays gradients consistent with the experimental trend at 15% and 120%, recapitulating the shear stiffening behaviour. The model can be calibrated to provide a good agreement with the experimental stress at high strain rates. However, when it is combined with the bond model, it fails nonetheless to capture the qualitative relationship between rupture strain and strain rate (**Fig. 7g**). This is to be expected as the lack of time-dependent behaviour implies that the rupture strain necessarily increases with the rupture stress, which increases with strain rate. The shear-stiffening behaviour of the network, therefore, appears to be required to account for the inverse correlation between the tension and strain at rupture. A possible interpretation for such a behaviour is that the keratin network is able to relax tension in a visco-elastic manner. Whenever a bundle of filaments is recruited as a result of the stretch, it would then behave not as an elastic component but as a Maxwell-like fluid, as a first order approximation. If we stretch faster than the relaxation time-scale of this system, all filaments can be recruited and the strain-stiffening is visible; whereas if we stretch slower, relaxation occurs faster than the rate at which new filaments are recruited and the stiffening behaviour is not observed. To implement this, we considered a material model consisting of many Maxwell branches in parallel, all identical but recruited at different strain thresholds (**Fig. 7h**). This non-linear visco-elastic model reproduces both the strain-stiffening at high strain rate and the shear-stiffening behaviour (**Fig. 7h - j**). The combined rheological and bond model shows a remarkable agreement with the experimental data for both rupture tension, strain, and time (**Fig. 7h - m**).

The relationship between rupture tension and rupture strain (**Fig. 7h**) connects two qualitatively different domains. At high rates, the rupture tension is large and the rupture strain is relatively low and constant. This is a regime where intermediate filament bundles are massively recruited, forcefully breaking the bonds. At slow rates, the rupture tension is smaller but the material is able to achieve much larger deformations before failing. This is associated with significant dissipation of stress in the intermediate filament network, keeping the tension lower and delaying the onset of fracture. When the intermediate filament network is disrupted, the rheology would be expected to be largely determined by the actomyosin network instead. Interestingly, the experimental rupture data of the K14-R125C monolayers clusters around the tension-strain curves extrapolated from

the low deformation regimes, known to be controlled by actomyosin [20] (**Fig. 7n**). This further supports the view that the keratin network is a key player controlling the onset of fracture in healthy monolayers.

Discussion

We have characterised fracture in epithelial monolayers and showed that they are remarkably strong, withstanding several-fold increases in length before the initiation of cracking. Remarkably, increases in cell contractility also ruptured monolayers in the absence of any applied deformation. By systematically varying strain rate, we reveal a trade-off between rupture tension and rupture time with large tensions leading to short lifetimes. Interestingly, rupture originating from contractility was consistent with experiments applying deformation at low strain rate, suggesting that active stresses arising from myosin contractility and passive stresses due to deformation of the cytoskeleton may be interchangeable. Importantly, we unravelled a role for the supracellular keratin filament network in controlling the rheology and strength of tissues. Finally, using computational modelling, we show that fracture onset depends strongly on tissue rheology and collective bond kinetics under force.

Our experiments revealed a key role for keratin intermediate filaments in the response of tissues to large deformations: they governed strain stiffening and protected monolayers against early rupture. Importantly, perturbing the keratin intermediate filaments directly or indirectly by disrupting their interfacing to desmosomes had the same qualitative effect, signifying that it is the supracellular network linking individual keratin networks that is important in these processes. Whereas the actomyosin cytoskeleton is central to cell and tissue mechanics at low strain [46, 47, 20], its perturbation did not affect strain stiffening nor the strength of tissues. These data paint a picture where the actomyosin cytoskeleton controls tissue rheology for deformations smaller than 50% and keratin intermediate filaments dominate for strains above 100%, consistent with previous work [31]. This transition was manifested by a progressive stiffening of monolayers for strain above 50%. Interestingly, such a mechanism was not observed in previous work examining the response of epithelia to large deformation [31], perhaps because of the much longer time-scales over which these experiments were performed (tens of hours). The exact mechanism through which strain stiffening arises remains to be determined. However, we hypothesise that it could be due to progressive tensile loading of keratin bundles with increasing deformation in a rate-dependent manner. Previous work has shown that, at low strain, keratin intermediate filament bundles appear wavy but straighten when deformation increases [31, 37]. Within cells, the keratin network radiates from the cell centroid towards the cell junctions [48] (**Fig. 5c**, first row). Therefore, in response to uniaxial stretch, keratin filaments aligned with the direction of stretch will straighten first and, as deformation increases, filaments at increasingly larger angles from this direction will straighten. Thus, more and more mechanical elements bear load as deformation increases. During physiological function, strain stiffening may help epithelia limit how much they deform in response to force application. Indeed, with strain stiffening, each additional increment in deformation necessitates the application of a larger increment in force.

Our experiments show that strain stiffening is strain rate dependent. This signifies that, at low strain rate, strain stiffening is absent and this may allow tissues to deform substantially. The molecular mechanism underlying strain rate dependency remains unclear, however, we hypothesise that it might involve molecular turnover of proteins within the keratin-desmosome force chain or sliding between filaments within the keratin bundles that link desmosomes to the cell centre. Indeed,

analysis of the buckling of keratin bundles within cells suggests the presence of sliding between filaments [33]. Stress dissipation at low strain arises from turnover to actomyosin [49, 20]. A similar mechanism may be at play for keratin intermediate filament networks. Monolayers subjected to 0.1% s^{-1} do not strain-stiffen. In these conditions, reaching the strain regime where stiffening is observed would necessitate $\sim$ 10 - 20 minutes. Therefore for turnover of a protein to participate in stress dissipation, it would need to take place over shorter times than this. While keratins and desmosomes turn over with characteristic times of $\sim$ 1h [50], the desmosomal cadherin desmoglein 2 displays substantially faster turnover on a time-scale of $\sim$ 20 minutes [51]. Future work will be necessary to determine which of sliding and turnover contributes most to stress dissipation in keratin networks.

Together our experiments and modelling allowed to link rupture of bonds at the molecular-scale to cellular forces arising from tissue-scale deformation of the monolayer. While the trade-off between force and lifetime was expected from previous work [23], our experiments indicate that tissue rheology plays an integral part in defining fracture characteristics. Remarkably, our model shows that prediction of rupture tension and strain necessitates the implementation of a realistic tissue rheology that incorporates shear stiffening. Our data poses an intriguing question. At high strain, wild-type monolayers strain stiffen and as a result, their tension is larger than monolayers with a perturbed keratin network. If the number of adhesion proteins linking the cells remains the same in both conditions, the force that each bond must bear will be larger in wild-type tissues than in K14-R125C monolayers. As a consequence, we would expect wild-type tissues to rupture at lower strains than keratin compromised ones, the contrary of what we observe. One potential explanation may be that desmosomal cadherins or desmosomal proteins possess catch-bond properties, similar to E-cadherin and alpha-catenin [52, 53]. At zero force, catch bonds have a very short lifetime but, as applied force increases, their lifetime grows to an optimum before decreasing again. Work using FRET tension sensors has shown that, under resting conditions in adherent monolayers, adherens junctions are under tension but that desmosomes are not [29, 35]. Thus, at low strain, desmosomal cadherins may not sense any force and have a lifetime so short that their contribution to intercellular adhesion is minimal. As strain increases, keratin filaments become progressively loaded, exerting tension on desmosomes and potentially increasing the lifetime of desmosomal cadherins as well as their contribution to load bearing. Thus, stretch would lead to both strain stiffening and an increase in the effective intercellular adhesion. In support of such a mechanism, RNAseq data indicates that the level of transcripts for E-cadherin, desmoglein 2, and desmocollin 2 are comparable in MDCK cells (**Table S6**). Furthermore, our model indicates that rupture stress decreases with decreasing number of bonds (**Fig. 7o**). However, we note that other changes to the model parameters (such as the slip bond characteristic force or the scale of the rate constants) can also lead to similar decreases in rupture stress (**Fig. 7o**). Future work will need to examine these hypotheses.

From a physiological point of view, the shear-stiffening behaviour enables the tissue to respond very differently to mechanical perturbations depending on the time-scale (**Fig. 7p**). The tissue responds to a fast, shock-like, perturbation by stiffening, therefore limiting the deformation and maximising the force at which the material fails. However, when subjected to a slow and steady deformation, the material can tolerate very large stretch without failure. This is, to our knowledge, the first characterisation of such a dynamic transition with regards to fracture behaviour.

In summary, our work has shown that the mechanics of tissues at high strain and high strain rate is dominated by a supracellular network of keratin intermediate filaments linked by desmosomes. This network protects monolayers from rupture by limiting deformation through strain stiffening and may also increase intercellular adhesion. One implication of our work is that the fracture characteristics of monolayers expressing K14-R125C reflect the fracture signature of actomyosin and adherens junctions, while the fracture characteristics of monolayers treated with latrunculin reflect the fracture signature of keratins and desmosomes. In the present study, we only examined the onset of rupture and future work will be needed to investigate crack propagation in the plane of the tissue.

Figures

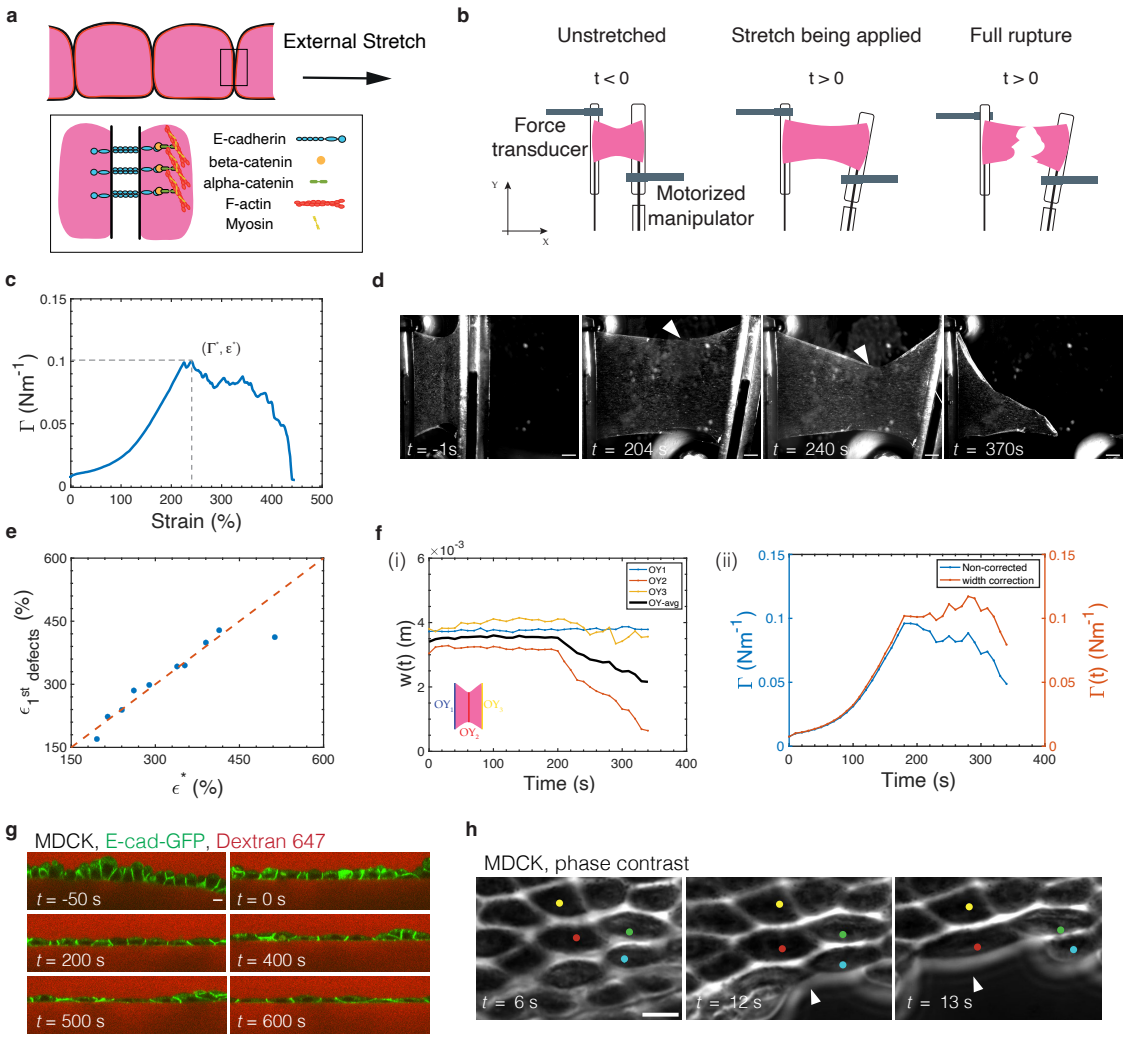
a
External Stretch
E-cadherin
beta-catenin
alpha-catenin
F-actin
Myosin
b
Unstretched
Stretch being applied
Full rupture
t < 0
t > 0
t > 0
Force transducer
Motorized manipulator
c
Γ (Nm⁻¹)
Strain (%)
d
t = -1s
t = 204 s
t = 240 s
t = 370s
e
ε 1st defects (%)
ε* (%)
f
(i)
w(t) (m)
Time (s)
OY1
OY2
OY3
OY-avg
(ii)
Γ (Nm⁻¹)
Γ(t) (Nm⁻¹)
Non-corrected
width correction
Time (s)
g
MDCK, E-cad-GFP, Dextran 647
t = -50 s
t = 0 s
t = 200 s
t = 400 s
t = 500 s
t = 600 s
h
MDCK, phase contrast
t = 6 s
t = 12 s
t = 13 s

Figure 1: Epithelial monolayers rupture in response to excessive stretch. a, Cellular-scale diagram of the monolayer profile. Top: profile view of the monolayer. Cells are linked to one another via specialised junctions. Bottom: zoom of an adherens junctions linking the F-actin cytoskeleton of neighbouring cells. The ectodomain of E-cadherin links cells to one another while its intracellular domain binds to the F-actin cytoskeleton via beta- and alpha-catenin. Myosin motor proteins bind F-actin to generate a cellular surface tension which results in a pre-tension in the monolayer. **b,** Diagram of the experiment. Monolayers in pink are subjected to a ramp in deformation applied via displacement of one of the test rods. Stretch starts at time 0 and continues at a constant rate until full rupture of the monolayer. **c,** Representative evolution of monolayer tension as a function of applied strain. Dashed lines show the maximum tension Γ^* and strain ϵ^* before appearance of the first defects. Full rupture of the monolayer takes place for $\epsilon = 450\%$. **d,** Bright-field microscopy time series of a ramp in deformation performed at 1% s^{-1}. Arrowheads indicate the crack tip. Time is indicated in the top right corner. Scale bar = 500 µm. **e,** Strain at which the first defects $\epsilon_{1^{\text{st}}\text{defects}}$ are observed as a function of the strain at which the maximum tension is reached ϵ^*. The dashed red line shows the line of slope 1. **f,** Crack front propagation occurs at a roughly constant tension. (i) Monolayer width as a function of time for a monolayer deformed at a strain rate of 1% s^{-1}. The average width of the monolayer OY_{avg} is shown in black and is computed from the width at each of the arms of the device, OY_1, OY_3 and the width at the middle of the monolayer OY_2. (ii) Force normalised to the initial monolayer width at time 0 (w_0, blue curve) and to the width at time t ($w(t)$, red curve) plotted as a function of time. The two curves coincide until the appearance of the first defects. After this, the red curve stays fairly constant over time. **g,** Time series of a profile view of a monolayer during stretch. Intercellular junctions are visualised with E-cadherin-GFP (green) and cells are visualised by dye exclusion of AlexaFluor 647-dextran (red) added to the medium. Time is indicated in the top right corner of each image. Deformation starts at time 0 at a rate of 1% s^{-1}. Scale bar = 10 µm. **h,** High magnification time series of crack propagation along cellular interfaces. The crack front is indicated by white arrowheads. Several cells are marked by coloured dots in each frame. Time is indicated in the top right corner. Scale bar = 10 µm.

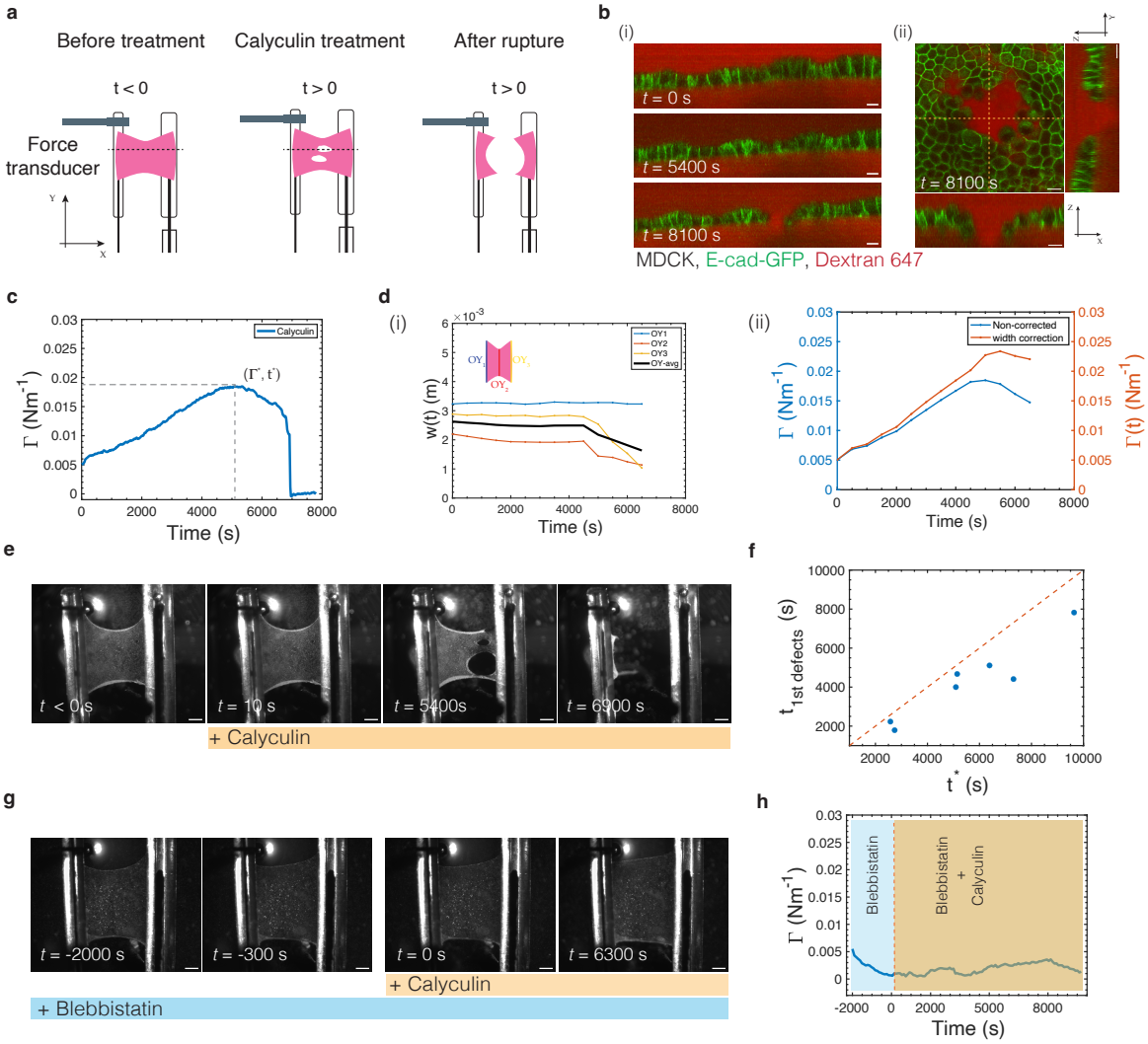
a
Before treatment
Calyculin treatment
After rupture
t < 0
t > 0
t > 0
Force transducer
b
(i)
(ii)
t = 0 s
t = 5400 s
t = 8100 s
t = 8100 s
MDCK, E-cad-GFP, Dextran 647
c
Calyculin
(Γ*, t*)
Γ (Nm-1)
Time (s)
d
(i)
OY1
OY2
OY3
OY-avg
w(t) (m)
Time (s)
(ii)
Non-corrected
width correction
Γ (Nm-1)
Γ(t) (Nm-1)
Time (s)
e
t < 0 s
t = 10 s
t = 5400s
t = 6300 s
+ Calyculin
f
t1st defects (s)
t* (s)
g
t = -2000 s
t = -300 s
t = 0 s
t = 6300 s
+ Calyculin
+ Blebbistatin
h
Blebbistatin
Blebbistatin + Calyculin
Γ (Nm-1)
Time (s)

Figure 2: Monolayers can self rupture by increasing their myosin contractility. a, Diagram of the experiment. Monolayers were treated with calyculin, an inhibitor of myosin phosphatase at t = 0. The tension in the monolayer was measured over time and the length of the monolayer was kept constant by the micromanipulator. After some time, defects appeared in the monolayer and measurements were continued until the monolayer failed. The dashed black line indicates a position from which a profile would be sampled such as the one displayed in b. **b,** Representative confocal images of a monolayer during calyculin treatment (time > 0). Intercellular junctions are visualised with E-cadherin-GFP (green) and cells are visualised by dye exclusion of AlexaFluor 647-dextran (red) added to the medium. Scale bar = 10 µm. (i) Profile views over time. Time is indicated in the top left corner of each image. (ii) XY view of a defect in a monolayer and its corresponding profile views in XZ and YZ. Dashed yellow lines indicate the position of the profile views. Time is indicated in the top left corner. **c,** Representative temporal evolution of tension in a calyculin-treated monolayer. The dashed lines indicate the maximum tension Γ^* and its timing t^*. **d,** Crack front propagation occurs at a roughly constant tension. (i) Monolayer width as a function of time for treated with calyculin. The average width of the monolayer $\mathrm{OY_{avg}}$ is shown in black and is computed from the width at each of the arms of the device, $\mathrm{OY_1}$, $\mathrm{OY_3}$ and the width at the middle of the monolayer $\mathrm{OY_2}$. (ii) Force normalised to the initial monolayer width at time 0 (w_0, blue curve) and to the width at time t ($w(t)$, red curve) plotted as a function of time. The two curves coincide until the appearance of the first defects. After this, the red curve stays fairly constant over time. **e,** Bright field time series showing a representative calyculin-treated monolayer. Calyculin is added to the medium at time 0. Time is indicated in the top left corner. Scale bar = 500 µm. **f,** Time at which the first defects $t_{1^{\mathrm{st}}\mathrm{defects}}$ are observed as a function of the time at which the maximum tension is reached t^*. The dashed red line shows the line of slope 1. **g,** Bright field time series of a representative monolayer treated with blebbistatin and calyculin. Calyculin was added at time 0. Blebbistatin treatment was started at t = -2000 s and the drug was present throughout the experiment. Scale bar = 500 µm. **h,** Temporal evolution of tension evolution in a monolayer treated with blebbistatin and calyculin. The monolayer was first treated with blebbistatin alone for 2000 s (blue shaded region) before calyculin was added (orange shaded region).

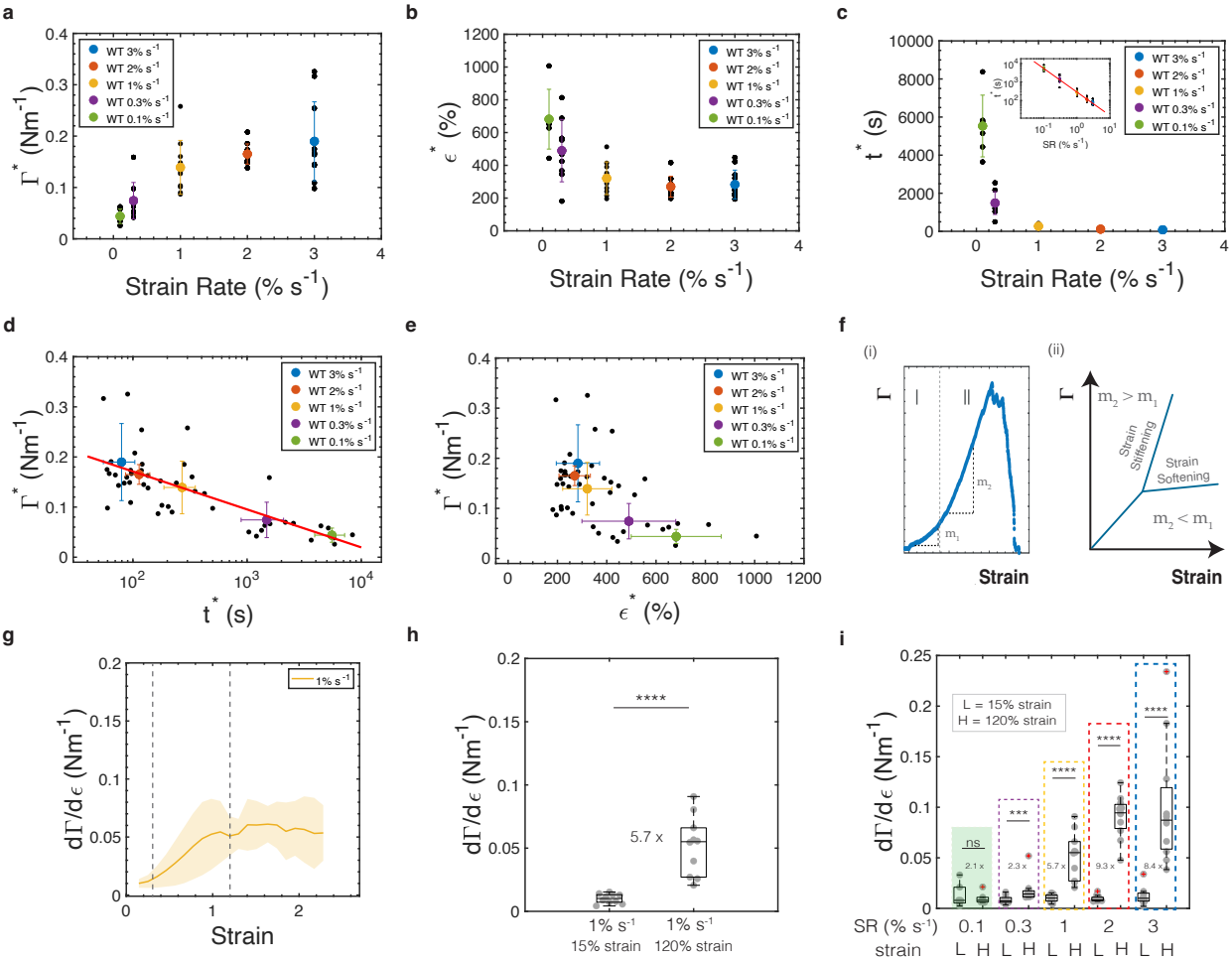
a
b
c
d
e
f
g
h
i
WT 3% s-1
WT 2% s-1
WT 1% s-1
WT 0.3% s-1
WT 0.1% s-1
Strain Rate (% s-1)
Γ* (Nm-1)
ϵ* (%)
t* (s)
SR (% s-1)
(i)
(ii)
Strain
m2 > m1
m2 < m1
Strain Stiffening
Strain Softening
1% s-1
dΓ/dϵ (Nm-1)
5.7 x
****
1% s-1 15% strain
1% s-1 120% strain
L = 15% strain
H = 120% strain
ns
***
SR (% s-1)
strain
0.1
0.3
1
2
3
L H L H L H L H L H

Figure 3: Rupture characteristics depend on strain rate. In box plots, the median of the distributions, the 25th and 75th percentiles, and the most extreme data points without outliers are represented by the central bars, the bounding boxes, and the whiskers, respectively. Outliers are shown with a red '+' symbol. Statistically significant difference was determined using a Kolmogorov-Smirnov-test: ns, non significant, ***P < 0.001, ****P < 0.0001.
a, Rupture tension, **b,** rupture strain and **c,** rupture time as functions of the strain rate. Inset in c, log-log representation. **d,** Rupture tension as a function of the rupture time. The graph is plotted on a semi-log scale because of the large range of time-scales associated with the different strain rates. The red line is a linear fit to the experimental data. **e,** Rupture tension as a function of rupture strain. In figs. **a - e** black dots represent individual monolayers. Coloured dots represent the average value and whiskers represent the standard deviations for a given strain rate. **f,** Monolayers display a strain stiffening behaviour above 50% strain. (i) Diagram showing the change in slope of a tension-strain curve, characteristic of the strain stiffening behaviour observed in monolayers. The dashed line indicates the approximate change in regime. The slope m2 observed at higher strain (region II) is larger than that the slope m1 observed at lower strain (region I). (ii) Example showing the difference in the tension-strain curve for a material that stiffens (slope increases) or one that softens (slope decreases above a threshold strain). **g,** Tension gradient as a function of strain for monolayers subjected to a ramp in deformation at 1% s^{-1}. The average value is represented by the thick line and the shaded area shows the standard deviation. The dashed lines show the strains at which gradients were measured for comparison between low strain and high strain (n = 10 monolayers). **h,** Tension gradient at low strain ($\epsilon = 15\%$, n = 10 monolayers) and at high strain ($\epsilon = 120\%$, n = 10 monolayers) from experiments pooled in panel **g**. The fold change is indicated between the two box plots. **i,** Tension gradient at low strain (L $\simeq$ 15%, n = 10) and at high strains (H $\simeq$ 120% n = 10) as a function of strain rate (n = 6 monolayers for 0.1% s^{-1}, n = 9 for 0.3% s^{-1} , n = 10 for 1% s^{-1}, n = 11 for 2% s^{-1}, n = 11 for 3% s^{-1}). The fold change for each strain rate is indicated between the low and high strain box plots.

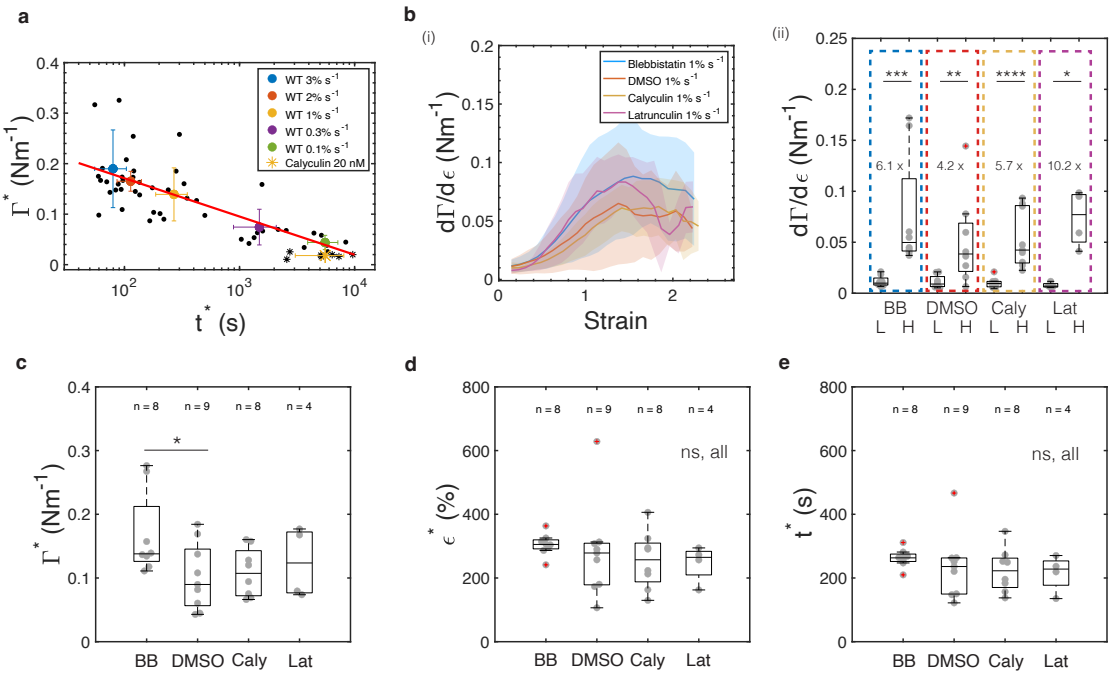
a
WT 3% s-1
WT 2% s-1
WT 1% s-1
WT 0.3% s-1
WT 0.1% s-1
Calyculin 20 nM
Γ* (Nm-1)
t* (s)
b
(i)
Blebbistatin 1% s-1
DMSO 1% s-1
Calyculin 1% s-1
Latrunculin 1% s-1
dΓ/dϵ (Nm-1)
Strain
(ii)
***
**
****
*
6.1 x
4.2 x
5.7 x
10.2 x
BB DMSO Caly Lat
L H L H L H L H
c
n = 8 n = 9 n = 8 n = 4
*
BB DMSO Caly Lat
d
n = 8 n = 9 n = 8 n = 4
ns, all
ϵ* (%)
e
n = 8 n = 9 n = 8 n = 4
ns, all
t* (s)

Figure 4: Strain stiffening does not depend on the actomyosin cytoskeleton. In box plots, the median of the distributions, the 25th and 75th percentiles, and the most extreme data points without outliers are represented by the central bars, the bounding boxes, and the whiskers, respectively. Outliers are shown with a red '+' symbol. Statistically significant difference was determined using a Kolmogorov-Smirnov-test: ns, non significant, *P < 0.05, **P < 0.01, ***P < 0.001, ****P < 0.0001.

a, Semi-log graph of the rupture tension as a function of the rupture strain for all strain rates (0.1% s^{-1} n = 6, 0.3% s^{-1} n = 9, 1% s^{-1} n = 10, 2% s^{-1} n = 11, 3% s^{-1} n = 11 monolayers) and for calyculin-treated monolayers (n = 7 monolayers). Note that the latter falls very close to the trend line expected for experiments in which strain rate is varied. **b,** Tension gradient for monolayers in which actomyosin has been perturbed. (i) Average tension gradient (thick lines) and standard deviation (shaded area) as a function of strain for ramp experiments performed at 1% s^{-1} for monolayers pre-incubated with blebbistatin 50 µM (blue, n = 8), DMSO (red, n = 9), calyculin 20 nM (yellow, n = 8) and latrunculin 1 µM (purple, n = 4). (ii) Box plots comparing the tension gradient at low strain (L $\simeq$ 15% strain) and high strain (H $\simeq$ 120 % strain) for monolayers treated with drugs perturbing the actomyosin cytoskeleton. **c - d,** Box plots for the **c,** rupture tension, **d,** rupture strain, and **e,** rupture time for monolayers pre-incubated with different treatments perturbing the actomyosin cytoskeleton.

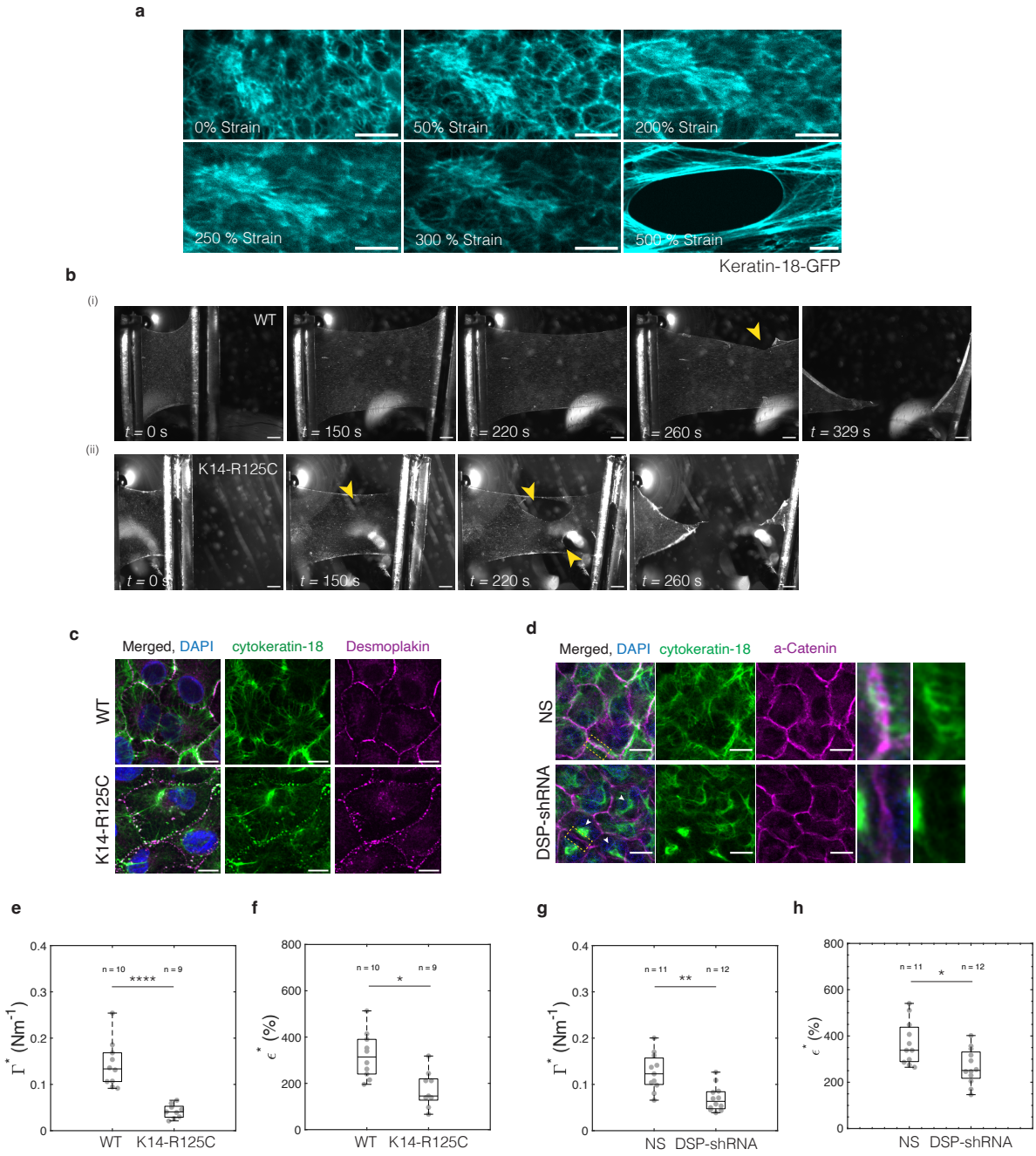
a
0% Strain
50% Strain
200% Strain
250 % Strain
300 % Strain
500 % Strain
Keratin-18-GFP
b
(i)
WT
t = 0 s
t = 150 s
t = 220 s
t = 260 s
t = 329 s
(ii)
K14-R125C
t = 0 s
t = 150 s
t = 220 s
t = 260 s
c
Merged, DAPI
cytokeratin-18
Desmoplakin
WT
K14-R125C
d
Merged, DAPI
cytokeratin-18
a-Catenin
NS
DSP-shRNA
e
f
g
h
Γ* (Nm-1)
ϵ* (%)
n = 10
n = 9
n = 11
n = 12
****
*
**
WT
K14-R125C
NS
DSP-shRNA

Figure 5: Perturbation of the keratin intermediate filament network fragilises monolayers. **a,** Image series of Keratin-18-GFP in cells in suspended monolayers subjected to increasing deformation. The strain is indicated in the bottom left corner. Scale bar = 10 µm. **b,** Bright-field time series of (i) representative WT and (ii) K14-R125C monolayers during a ramp experiment performed at 1% s^{-1}. Arrowheads indicate the start and growth of the cracks. Time is indicated in the bottom left corner. Scale bar = 500 µm. **c, d,** In all panels, the leftmost column shows an overlay. Nuclei are shown in blue in all panels. Scale bar is 10 µm. **c,** Immunostaining of cytokeratin-18 (green) and desmoplakin (magenta) in WT (top row) and K14-R125C monolayers (bottom row). **d,** Immunostaining of cytokeratin-18 (green) and α-catenin (magenta) in NS control (top row) and DSP-shRNA monolayers (bottom row). Right panels show a zoom around the intercellular junction within the yellow dashed box. White arrowheads show cells in which the keratin network is condensed around the nucleus. **(e - h)** Box plots comparing **e, g** rupture tension and **f, h** rupture strain between WT and K14-R125C monolayers and control (NS) with Desmoplakin-shRNA (DSP-shRNA) monolayers respectively. Statistically significant difference: *P $<$ 0.05, **P $<$ 0.01, ****P $<$ 0.0001, Kolmogorov-Smirnov-test.

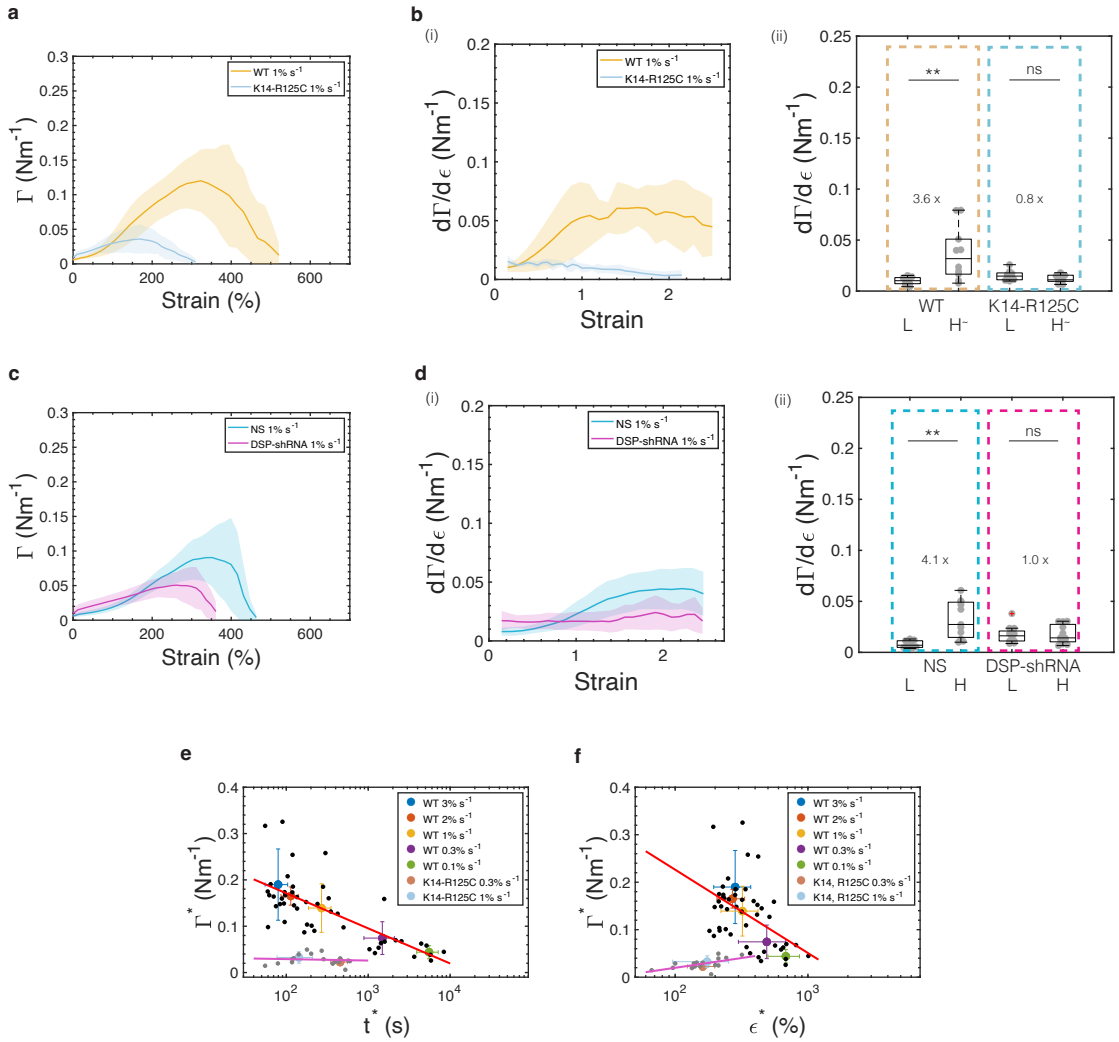
a
Γ (Nm-1)
Strain (%)
WT 1% s-1
K14-R125C 1% s-1
b
(i)
dΓ/dϵ (Nm-1)
Strain
(ii)
**
ns
3.6 x
0.8 x
WT
K14-R125C
L
H-
c
NS 1% s-1
DSP-shRNA 1% s-1
d
4.1 x
1.0 x
NS
DSP-shRNA
H
e
f
WT 3% s-1
WT 2% s-1
WT 1% s-1
WT 0.3% s-1
WT 0.1% s-1
K14-R125C 0.3% s-1
K14-R125C 1% s-1
K14, R125C 0.3% s-1
K14, R125C 1% s-1
t* (s)
ϵ* (%)

Figure 6: Keratin intermediate filament networks within cells are highly deformable. In box plots the median of the distributions, the 25th and 75th percentiles, and the most extreme data points without outliers are represented by the central bars, the bounding boxes, and the whiskers, respectively. Outliers are shown with a red '+' symbol. Statistically significant difference between groups was performed using a Kolmogorov-Smirnov-test: ns, non significant $P > 0.05$, $^{**}P < 0.01$.

a, Tension-Strain curves for WT (yellow, n = 10) and K14-R125C (blue, n = 9) monolayers subjected to ramps in deformation at 1% s^{-1}. Solid lines represent the average value and shaded areas the standard deviation. **b,** Tension gradient for WT and K14-R125C monolayers. (i) Average tension gradient (solid lines) of K14-R125C monolayers (blue, n = 9) and WT monolayers (yellow, n = 10). Shaded areas show the standard deviation. (ii) Box plots of the tension gradient at low (L $\simeq$ 15% strain) and high strain ($H^{\sim}$ $\simeq$ 70% strain) in WT and K14-R125C monolayers. The fold change between low and high strains is indicated in between the box plots. **c,** Tension-Strain curves for NS control (cyan, n = 11) and DSP-shRNA (magenta, n = 12) monolayers subjected to ramps in deformation at 1% s^{-1}. Solid lines represent the average value and shaded areas the standard deviation. **e,** Graph showing rupture tension as a function of rupture time and **f,** rupture tension as a function of rupture strain in response to external stretch for WT (black dots) and K14-R125C (grey dots) monolayers. Data points are acquired for different strain rates. Coloured dots show the population average for a given strain rate (0.1% s^{-1} n = 6, 0.3% s^{-1} n = 9, 1% s^{-1} n = 10, 2% s^{-1} n = 11, 3% s^{-1} n = 11 for WT monolayers. 0.3% s^{-1} n = 8, 1% s^{-1} n = 9, for K14,R125C monolayers).

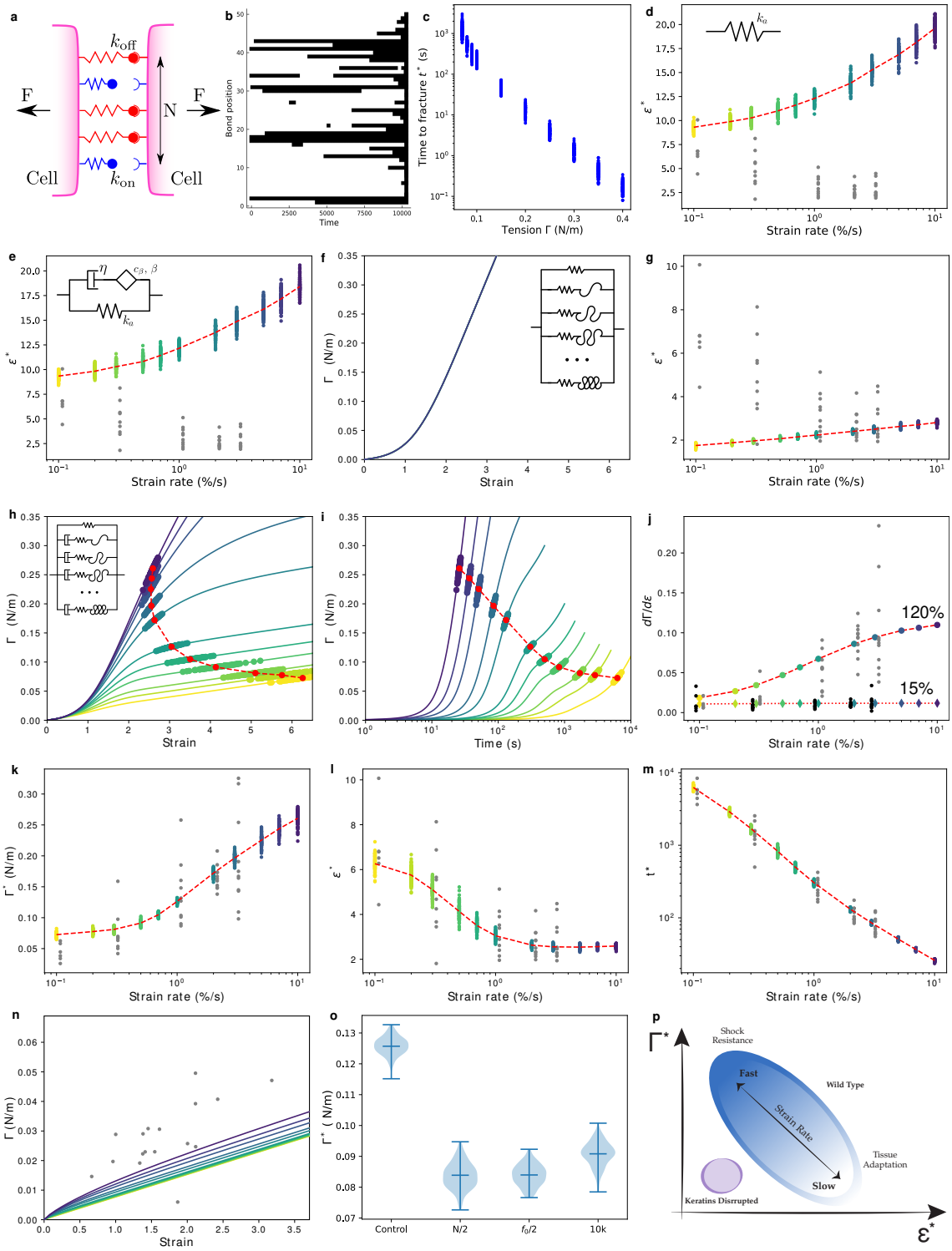
a
F
F
N
Cell
Cell
k_{off}
k_{on}
b
Bond position
Time
c
Time to fracture t^* (s)
Tension Γ (N/m)
d
k_a
ε^*
Strain rate (%/s)
e
η
c_β, β
k_a
ε^*
Strain rate (%/s)
f
Γ (N/m)
Strain
g
ε^*
Strain rate (%/s)
h
Γ (N/m)
Strain
i
Γ (N/m)
Time (s)
j
dΓ/dε
120%
15%
Strain rate (%/s)
k
Γ* (N/m)
Strain rate (%/s)
l
ε^*
Strain rate (%/s)
m
t^*
Strain rate (%/s)
n
Γ (N/m)
Strain
o
Γ* (N/m)
Control
N/2
f_0/2
10k
p
Γ*
Shock Resistance
Fast
Wild Type
Strain Rate
Tissue Adaptation
Slow
Keratins Disrupted
ε*

Figure 7: Multiscale modelling of fracture onset. (**d-e**, **g-m**) Each coloured dot represents a simulation run. 100 simulations were run for each strain rate. Each grey dot represents an experimental data point. The dashed and dotted red lines link the mean value for each strain, strain rate, or time to show the trend.

a, Cell surfaces are linked by a population of N independent linkers with slip bond dynamics and subjected to a force F. Each linker can associate with its counterpart on the opposite surface with a rate constant k_{on} and dissociate with a rate constant k_{off}. The latter depends on the force f it is subjected to: $k_{off} = k_{off,0}e^{f/f_0}$ where f_0 is a model parameter. The total force applied to the surface is assumed equally shared between closed bonds. **b,** Typical evolution of the states of a population of 50 links over time when the junction is subjected to a constant tension. The black color indicates an unbound state. The simulation ends when all links are unbound, defining $t = t^*$. **c,** Time to fracture t^* as a function of the mechanical tension for junctions subjected to a constant tension. **d,** Strain at rupture as a function of the ramp strain rate for a linear elastic material. The inset represents the rheological model used. **e,** Strain at rupture as a function of the ramp strain rate for a linear visco-elastic material. The rheological model is shown in inset and is fitted to the rheology of wild-type MDCK monolayers at low strain [42]. **f,** Tension-strain relationship for a strain stiffening material. The rheological model is shown in inset and it accounts for the strain stiffening behaviour observed at large strains in the monolayer. **g,** Strain at rupture as a function of the ramp strain rate for a strain stiffening material. The rheological model is shown in **f**. **h,** Tension-strain, and **i,** tension-time characteristics (solid lines) for a shear stiffening material. The rheological model is presented as inset in **h**. Each curve represents a different strain rate. The colour code indicates the strain-rate consistently with panels **j-m**. Dark blue colours indicate large strain rates, while yellow colours indicate small strain rates. **j,** Tension gradient at 15% and 120% strain as a function of strain rate for a shear stiffening material. The rheological model is presented as an inset in **h**. Grey dots show experimental data at 120% and black dots at 15% strain. **k - m,** Graphs showing the **k,** tension, **l,** strain, and **m,** time, at rupture as a function of the ramp strain rate for the model presented in **h**. **n,** Tension as a function of strain for the linear viscoelastic model presented in panel **e**. Grey dots represent the rupture tension and rupture strain for K14-R125C monolayers. Each coloured solid line represents a different strain rate with the same colour code as **h**. **o,** Violin plots for the main bond model. The middle line shows the median and the whiskers the extremes. Effect of the main bond model on the rupture tension Γ^*, for a ramp at 1% s^{-1}. Reducing the number of bonds per-junction N by a factor 2 (N/2), reducing the force threshold f_0 in the slip bond behaviour by a factor two ($f_0/2$), or increasing the rates k_{on} and $k_{off,0}$ by a factor (10k) all lead to a significant reduction of the rupture tension. **p,** Summary diagram showing the range of behaviours displayed by monolayers. Wild-type monolayers (blue region) subjected to ramps at high strain rates have a high rupture tension and low rupture strain, making them an ideal material to resit shocks. At low strain rates, the rupture strain is large and the rupture stress is low, allowing the material to adapt. Disruption of keratin intermediate filaments abrogates these strain rate-dependent behaviours.

References

[1] Matthew A Caporizzo and Benjamin L Prosser. Need for speed: the importance of physiological strain rates in determining myocardial stiffness. *Frontiers in physiology*, page 1183, 2021.

[2] Jeffrey J Fredberg, David Inouye, Brett Miller, Madhavi Nathan, Samah Jafari, Soufia Helioui Raboudi, James P Butler, and Stephanie A Shore. Airway smooth muscle, tidal stretches, and dynamically determined contractile states. *American journal of respiratory and critical care medicine*, 156(6):1752–1759, 1997.

[3] Raman Maiti, Lutz-Christian Gerhardt, Zing S Lee, Robert A Byers, Daniel Woods, José A Sanz-Herrera, Steve E Franklin, Roger Lewis, Stephen J Matcher, and Matthew J Carré. In vivo measurement of skin surface strain and sub-surface layer deformation induced by natural tissue stretching. *journal of the mechanical behavior of biomedical materials*, 62:556–569, 2016.

[4] Edward W Obropta and Dava J Newman. A comparison of human skin strain fields of the elbow joint for mechanical counter pressure space suit development. In *2015 IEEE Aerospace Conference*, pages 1–9. IEEE, 2015.

[5] Pierre A Coulombe and M Bishr Omary. 'hard'and 'soft'principles defining the structure, function and regulation of keratin intermediate filaments. *Current opinion in cell biology*, 14(1):110–122, 2002.

[6] AD Irvine and WHI McLean. Human keratin diseases: the increasing spectrum of disease and subtlety of the phenotype–genotype correlation. *British Journal of Dermatology*, 140(5):815–828, 1999.

[7] TT Shih and J Opoku. Application of fracture mechanics to ceramic materials—a state-of-the-art review. *Engineering Fracture Mechanics*, 12(4):479–498, 1979.

[8] A. Pineau, A.A. Benzerga, and T. Pardoen. Failure of metals i: Brittle and ductile fracture. *Acta Materialia*, 107:424–483, 2016.

[9] Costantino Creton and Matteo Ciccotti. Fracture and adhesion of soft materials: a review. *Reports on Progress in Physics*, 79(4):046601, mar 2016.

[10] Rong Long, Chung-Yuen Hui, Jian Ping Gong, and Eran Bouchbinder. The fracture of highly deformable soft materials: A tale of two length scales. *Annual Review of Condensed Matter Physics*, 12(1):71–94, 2021.

[11] Alessandra Bonfanti, Julia Duque, Alexandre Kabla, and Guillaume Charras. Fracture in living tissues. *Trends in Cell Biology*, 2022.

[12] Amsha Proag, Bruno Monier, and Magali Suzanne. Physical and functional cell-matrix uncoupling in a developing tissue under tension. *Development*, 146(11):dev172577, 2019.

[13] Vivek N Prakash, Matthew S Bull, and Manu Prakash. Motility-induced fracture reveals a ductile-to-brittle crossover in a simple animal's epithelia. *Nature Physics*, 17(4):504–511, 2021.

[14] Julien G Dumortier, Mathieu Le Verge-Serandour, Anna Francesca Tortorelli, Annette Mielke, Ludmilla de Plater, Hervé Turlier, and Jean-Léon Maître. Hydraulic fracturing and active coarsening position the lumen of the mouse blastocyst. *Science*, 365(6452):465–468, 2019.

[15] Chii Jou Chan, Maria Costanzo, Teresa Ruiz-Herrero, Gregor Mönke, Ryan J Petrie, Martin Bergert, Alba Diz-Munoz, L Mahadevan, and Takashi Hiiragi. Hydraulic control of mammalian embryo size and cell fate. *Nature*, 571(7763):112–116, 2019.

[16] Yukiko Nakaya and Guojun Sheng. Epithelial to mesenchymal transition during gastrulation: an embryological view. *Development, growth & differentiation*, 50(9):755–766, 2008.

[17] Julia Duque and Nicole Gorfinkiel. Integration of actomyosin contractility with cell-cell adhesion during dorsal closure. *Development*, 143(24):4676–4686, 2016.

[18] Johan De Rooij, Andre Kerstens, Gaudenz Danuser, Martin A Schwartz, and Clare M Waterman-Storer. Integrin-dependent actomyosin contraction regulates epithelial cell scattering. *The Journal of cell biology*, 171(1):153–164, 2005.

[19] Andrew R Harris, Julien Bellis, Nargess Khalilgharibi, Tom Wyatt, Buzz Baum, Alexandre J Kabla, and Guillaume T Charras. Generating suspended cell monolayers for mechanobiological studies. *Nature protocols*, 8(12):2516–2530, 2013.

[20] Nargess Khalilgharibi, Jonathan Fouchard, Nina Asadipour, Ricardo Barrientos, Maria Duda, Alessandra Bonfanti, Amina Yonis, Andrew Harris, Payman Mosaffa, Yasuyuki Fujita, et al. Stress relaxation in epithelial monolayers is controlled by the actomyosin cortex. *Nature physics*, 15(8):839–847, 2019.

[21] Tom PJ Wyatt, Jonathan Fouchard, Ana Lisica, Nargess Khalilgharibi, Buzz Baum, Pierre Recho, Alexandre J Kabla, and Guillaume T Charras. Actomyosin controls planarity and folding of epithelia in response to compression. *Nature materials*, 19(1):109–117, 2020.

[22] Tom PJ Wyatt, Andrew R Harris, Maxine Lam, Qian Cheng, Julien Bellis, Andrea Dimitracopoulos, Alexandre J Kabla, Guillaume T Charras, and Buzz Baum. Emergence of homeostatic epithelial packing and stress dissipation through divisions oriented along the long cell axis. *Proceedings of the National Academy of Sciences*, 112(18):5726–5731, 2015.

[23] Yuval Mulla, Giorgio Oliveri, Johannes TB Overvelde, and Gijsje H Koenderink. Crack initiation in viscoelastic materials. *Physical review letters*, 120(26):268002, 2018.

[24] Thorsten Erdmann and Ulrich S Schwarz. Stochastic dynamics of adhesion clusters under shared constant force and with rebinding. *The Journal of chemical physics*, 121(18):8997–9017, 2004.

[25] Cornelis Storm, Jennifer J Pastore, Fred C MacKintosh, Tom C Lubensky, and Paul A Janmey. Nonlinear elasticity in biological gels. *Nature*, 435(7039):191–194, 2005.

[26] Mingxi Yao, Wu Qiu, Ruchuan Liu, Artem K Efremov, Peiwen Cong, Rima Seddiki, Manon Payre, Chwee Teck Lim, Benoit Ladoux, René-Marc Mege, et al. Force-dependent conformational switch of α-catenin controls vinculin binding. *Nature communications*, 5(1):1–12, 2014.

[27] Shigenobu Yonemura, Yuko Wada, Toshiyuki Watanabe, Akira Nagafuchi, and Mai Shibata. α-catenin as a tension transducer that induces adherens junction development. *Nature cell biology*, 12(6):533–542, 2010.

[28] Katsutoshi Taguchi, Takashi Ishiuchi, and Masatoshi Takeichi. Mechanosensitive eplin-dependent remodeling of adherens junctions regulates epithelial reshaping. *Journal of Cell Biology*, 194(4):643–656, 2011.

[29] Nicolas Borghi, Maria Sorokina, Olga G Shcherbakova, William I Weis, Beth L Pruitt, W James Nelson, and Alexander R Dunn. E-cadherin is under constitutive actomyosin-generated tension that is increased at cell–cell contacts upon externally applied stretch. *Proceedings of the National Academy of Sciences*, 109(31):12568–12573, 2012.

[30] Marihan Hegazy, Abbey L Perl, Sophia A Svoboda, and Kathleen J Green. Desmosomal cadherins in health and disease. *Annual Review of Pathology: Mechanisms of Disease*, 17:47–72, 2022.

[31] Ernest Latorre, Sohan Kale, Laura Casares, Manuel Gómez-González, Marina Uroz, Léo Valon, Roshna V Nair, Elena Garreta, Nuria Montserrat, Aránzazu Del Campo, et al. Active superelasticity in three-dimensional epithelia of controlled shape. *Nature*, 563(7730):203–208, 2018.

[32] L Kreplak, H Bär, JF Leterrier, H Herrmann, and U Aebi. Exploring the mechanical behavior of single intermediate filaments. *Journal of molecular biology*, 354(3):569–577, 2005.

[33] Jens-Friedrich Nolting, Wiebke Möbius, and Sarah Köster. Mechanics of individual keratin bundles in living cells. *Biophysical journal*, 107(11):2693–2699, 2014.

[34] Charlotta Lorenz, Johanna Forsting, Anna V Schepers, Julia Kraxner, Susanne Bauch, Hannes Witt, Stefan Klumpp, and Sarah Köster. Lateral subunit coupling determines intermediate filament mechanics. *Physical review letters*, 123(18):188102, 2019.

[35] Andrew J Price, Anna-Lena Cost, Hanna Ungewiß, Jens Waschke, Alexander R Dunn, and Carsten Grashoff. Mechanical loading of desmosomes depends on the magnitude and orientation of external stress. *Nature communications*, 9(1):1–11, 2018.

[36] Pierre A Coulombe, Michelle L Kerns, Elaine Fuchs, et al. Epidermolysis bullosa simplex: a paradigm for disorders of tissue fragility. *The Journal of clinical investigation*, 119(7):1784–1793, 2009.

[37] Andrew R Harris, Loic Peter, Julien Bellis, Buzz Baum, Alexandre J Kabla, and Guillaume T Charras. Characterizing the mechanics of cultured cell monolayers. *Proceedings of the National Academy of Sciences*, 109(41):16449–16454, 2012.

[38] Melanie Homberg, Lena Ramms, Nicole Schwarz, Georg Dreissen, Rudolf E Leube, Rudolf Merkel, Bernd Hoffmann, and Thomas M Magin. Distinct impact of two keratin mutations causing epidermolysis bullosa simplex on keratinocyte adhesion and stiffness. *Journal of Investigative Dermatology*, 135(10):2437–2445, 2015.

[39] Kristin Seltmann, Fang Cheng, Gerhard Wiche, John E Eriksson, and Thomas M Magin. Keratins stabilize hemidesmosomes through regulation of β4-integrin turnover. *Journal of Investigative Dermatology*, 135(6):1609–1620, 2015.

[40] Wangsun Choi, Bipul R Acharya, Grégoire Peyret, Marc-Antoine Fardin, René-Marc Mège, Benoit Ladoux, Alpha S Yap, Alan S Fanning, and Mark Peifer. Remodeling the zonula adherens in response to tension and the role of afadin in this response. *Journal of Cell Biology*, 213(2):243–260, 2016.

[41] Joshua A Broussard, Ruiguo Yang, Changjin Huang, S Shiva P Nathamgari, Allison M Beese, Lisa M Godsel, Marihan H Hegazy, Sherry Lee, Fan Zhou, Nathan J Sniadecki, et al. The desmoplakin–intermediate filament linkage regulates cell mechanics. *Molecular biology of the cell*, 28(23):3156–3164, 2017.

[42] Alessandra Bonfanti, Jonathan Fouchard, Nargess Khalilgharibi, Guillaume Charras, and Alexandre Kabla. A unified rheological model for cells and cellularised materials. *Royal Society open science*, 7(1):190920, 2020.

[43] A Kabla and L Mahadevan. Nonlinear mechanics of soft fibrous networks. *Journal of The Royal Society Interface*, 4(12):99–106, 2007.

[44] RC Picu. Mechanics of random fiber networks—a review. *Soft Matter*, 7(15):6768–6785, 2011.

[45] Chase P Broedersz and Fred C MacKintosh. Modeling semiflexible polymer networks. *Reviews of Modern Physics*, 86(3):995, 2014.

[46] Charlène Guillot and Thomas Lecuit. Adhesion disengagement uncouples intrinsic and extrinsic forces to drive cytokinesis in epithelial tissues. *Developmental cell*, 24(3):227–241, 2013.

[47] Carl-Philipp Heisenberg and Yohanns Bellaïche. Forces in tissue morphogenesis and patterning. *Cell*, 153(5):948–962, 2013.

[48] Roy A Quinlan, Nicole Schwarz, Reinhard Windoffer, Christine Richardson, Tim Hawkins, Joshua A Broussard, Kathleen J Green, and Rudolf E Leube. A rim-and-spoke hypothesis to explain the biomechanical roles for cytoplasmic intermediate filament networks. *Journal of cell science*, 130(20):3437–3445, 2017.

[49] Elisabeth Fischer-Friedrich, Yusuke Toyoda, Cedric J Cattin, Daniel J Müller, Anthony A Hyman, and Frank Jülicher. Rheology of the active cell cortex in mitosis. *Biophysical journal*, 111(3):589–600, 2016.

[50] Reinhard Windoffer, Monika Borchert-Stuhlträger, and Rudolf E Leube. Desmosomes: interconnected calcium-dependent structures of remarkable stability with significant integral membrane protein turnover. *Journal of cell science*, 115(8):1717–1732, 2002.

[51] Minnah Thomas, Benoit Ladoux, and Yusuke Toyama. Desmosomal junctions govern tissue integrity and actomyosin contractility in apoptotic cell extrusion. *Current Biology*, 30(4):682–690, 2020.

[52] Sabyasachi Rakshit, Yunxiang Zhang, Kristine Manibog, Omer Shafraz, and Sanjeevi Sivasankar. Ideal, catch, and slip bonds in cadherin adhesion. *Proceedings of the National Academy of Sciences*, 109(46):18815–18820, 2012.

[53] C Arbore, M Sergides, L Gardini, G Bianchi, AV Kashchuk, I Pertici, P Bianco, FS Pavone, and M Capitanio. α-catenin switches between a slip and an asymmetric catch bond with f-actin to cooperatively regulate cell junction fluidity. *Nature communications*, 13(1):1–11, 2022.

[54] Johannes Schindelin, Ignacio Arganda-Carreras, Erwin Frise, Verena Kaynig, Mark Longair, Tobias Pietzsch, Stephan Preibisch, Curtis Rueden, Stephan Saalfeld, Benjamin Schmid, et al. Fiji: an open-source platform for biological-image analysis. *Nature methods*, 9(7):676–682, 2012.

[55] George I. Bell. Models for the specific adhesion of cells to cells. *Science*, 200(4342):618–627, 1978.

[56] Jonathan Louis Kaplan, Alessandra Bonfanti, and Alexandre Kabla. Rheos. jl-a julia package for rheology data analysis. *arXiv preprint arXiv:2005.02538*, 2020.

Acknowledgements

The authors thank past and present members of the Charras and Kabla labs for discussions. The authors acknowledge technical support in LabVIEW development from A. Lisica. JD and GC were supported by European Research Council consolidator grant (CoG-647186) and a sLOLA grant from the British Biotechnology and Biological Sciences Research council (BBSRC, BB/V019015/1) to GC. AB was supported by the seal of Excellence (SoE) fellowship from Politecnico di Milano. JF was supported by a grant from the BBSRC (BB/M003280 and BB/M002578) to GC and AK. AH was supported by a BBSRC grant (BB/K013521) to GC and AK. EF was supported by BBSRC grant (BB/V019015/1) to GC.

Author Contributions

J.D., J.F., A.K. and G.C. conceived the project and wrote the manuscript. J.D. performed most of the experiments, analysis, and microscopy. J.F. performed some experiments and provided experimental and analysis tools. A.H. established the initial methods and contributed some experiments. E.F. performed the Western blotting and helped with establishment of cell lines. G.C. contributed reagents and established some of the cell lines. A.B. and A.K. designed and implemented the model. A.K. advised on analysis. A.K. and G.C. oversaw the entire project and writing. All authors discussed the results and manuscript.

Competing interests

The authors declare no competing interests.

Data availability

All reagents are available from the corresponding author upon request. Code and primary data are available from the UCL data repository (https://rdr.ucl.ac.uk/).

Methods

Cell culture

MDCK cells were cultured at 37 °C in an atmosphere of 5% CO_2 in DMEM (1X) + Glutamax (Thermo Fisher) supplemented with 10% fetal bovine serum (FBS, Sigma-Aldrich), 2.5% of 1M HEPES buffer (Sigma-Aldrich) and 1% penicillin-streptomycin (Thermo Fisher). Cells were passaged at 1:5 ratio every 4 days using standard cell culture protocols and disposed of after 30 passages. Mechanical experiments were performed in Leibovitz's L15 without phenol red (Thermo Fisher) supplemented with 10% fetal bovine serum (FBS, Sigma-Aldrich), 2.5% of 1M HEPES buffer (Sigma-Aldrich) and 1% penicillin-streptomycin (Thermo Fisher). For imaging and mechanical testing, the culture medium was exchanged for imaging medium that consisted of Leibovitz L15 without phenol red (ThermoFisher) supplemented with 10% FBS.

To visualise junctional and cytoskeletal structures, we used stables lines expressing E-cadherin-GFP, Vinculin-GFP, EPLIN-GFP, and Keratin 18-GFP. Details about their generation are given in [20], [37]. Stable expression of the tagged protein of interest was ensured by antibiotic selection using either 250 ng/mL puromycin or 1 mg/mL G418.

To study the role of intermediate filaments, we generated cell lines stably expressing Keratin 14 R125C and depleted in Desmoplakin. The cDNA encoding Keratin 14 R125C-YFP was a kind gift of Thomas Magin (University of Leipzig, Germany) and was cloned into a retroviral vector (pTRE, Takara Clontech). Retrovirus was generated as described in [37] and transduced into MDCK cells. After 2 weeks selection with hygromycin (400 µg/mL), cells were sorted to achieve a homogenous level of fluorescence.

To knock down desmoplakin, we purchased shRNAs targeting dog desmoplakin in a lentiviral vector (V3LHS 302846 and 302847, pGIPZ vector, Horizon discovery, Perkin Elmer, UK). We generated lentiviral particles following manufacturer instructions, transduced MDCK cells, selected cells with puromycin and sorted the cells with flow cytometry to achieve a homogenous knock down. As a control, we also generated a cell line expressing non-silencing shRNA. Protein depletion was verified by immunoblotting (**Fig. S8**). The antibodies used were anti-desmoplakin (Progen) and with anti-GAPDH as a loading control (Abcam). Appropriate HRP-coupled secondary antibodies (dilution 1:10,000) were from Jackson ImmunoResearch and Cytiva. The shRNA used in this work was shRNA2 from **Fig. S8**.
None of the cell lines in this study were found in the database of commonly misidentified cell lines maintained by International Cell Line Authentication Committee and National Center for Biotechnology Information Biosample. All cell lines were cultured at 37 °C with 5% CO2. All lines were routinely screened for the presence of mycoplasma using the MycoALERT kit (Lonza).

RNA sequencing

We used mRNA sequencing (RNASeq) to quantify the normalised expression of mRNA transcripts for proteins in subcellular structures as described in [20]. Briefly, to prepare total RNA samples,

MDCK cells were cultured for 3 days to reach confluence. This provides sufficient time for the junctions to mature and for the mRNA content to be regulated. Next, the total RNA was extracted using Tri reagent (Sigma Aldrich) following the manufacturer's protocol.

Stress measurement devices

The stress measurement devices were an adaptation of the force measurement device described in [19]. Briefly, two nickel-titanium (nitinol) wires (Euroflex) with different stiffnesses were glued into a bent glass capillary (Sutter Instruments). The arm with the stiffer wire was covered by a glass capillary to create a reference rod and two Tygon cylinders were glued to the extremities of both wires.

Generation of suspended epithelial monolayers

Suspended epithelial monolayers were generated as described by [19]. Briefly, mechanical devices were glued into Petri dishes, placing a glass capillary underneath them to prevent contact between the device and the bottom of the Petri dish which creates friction. To maintain the distance between the rods constant during the preparation procedure, a custom-designed, 3D printed plastic holder was placed in between them.

Collagen was reconstituted on ice by mixing 50% of collagen (Cellmatrix type I-A, Nitta Gelatin), 20% of 5X DMEM, 20% of sterile water, and 10% of reconstitution buffer (50 mM NaOH solution in sterile water, 200 mM HEPES and 262 mM of $NaHCO_3$) following manufacturer instructions. A 10 µL drop of collagen was placed between the rods and left to solidify in a dry incubator at 37 °C for 1-1.5 h. Once a solid collagen scaffold was formed, the devices were rehydrated by placing an 8 µL drop of cell culture medium onto it and two 250 µL drops on the bottom of the dish. The dish was then placed for 30 min inside a humidified incubator at 37 °C. During the rehydration time, confluent flasks of MDCK cells were trypsinised for 20 min. Cells were then resuspended to a final concentration of 3×10^4 cells per 10 µL. After rehydration, a 10 µL drop of the resuspended cells was placed on top of the collagen scaffold; cells were left to settle onto the collagen for 30 min inside the incubator. After this time, 8 mL of medium was added to each Petri dish, and both the V-shaped glass capillary and the holder separator were gently removed. The devices were left in the incubator for 48 - 72 h to allow cells to grow to confluence, covering the collagen scaffold and part of the Tygon cylinders on each test rod.

Removal of the collagen substrate

Immediately prior to experimentation, a collagenase solution was prepared by mixing collagenase type-II (Worthington Biochemical) with imaging medium to reach a final concentration of 250 units per mL. This solution was gradually exchanged with the cell culture medium in the Petri dishes containing the devices and then left for 1 h at 37 °C to allow for full enzymatic digestion of the collagen. Finally, the collagenase solution was gradually replaced with imaging medium. The device was then ready to be used for experiments.

Mechanical testing procedure

The mechanical setup was mounted on the stage of an inverted microscope (Olympus IX-71) and is described in [20]. The stiffer rod of the device was brought into contact with the arm of a motorized manipulator (M126-DG1) controlled through a C-863 controller (Physik Instrumente) whereas the softer arm of the device was attached to the tip of the force transducer (SI-KG7A, World Precision Instruments) held in position by a manual micromanipulator. Both the motorized manipulator and the force transducer were mounted onto magnetic plates to secure them firmly onto the microscope stage. The motorized manipulator allowed us to subject monolayers to different strains with precise control of strain rate. Stretched monolayers exerted restoring forces on the flexible rod, deflecting the force transducer. This deflection was transformed into a voltage that was converted into a digital signal using a data acquisition system (USB-1608G, Measurement Computing) and recorded on a computer. The motorized manipulator was controlled using a custom-written code in Labview (National Instruments). During the experiment, images of the monolayer were taken every 1 s using a 2X objective (2X PLN Olympus) and a GS3-U3-60QS6M-C, Point Grey camera.

Quantification of tissue tension

In experiments using suspended epithelial monolayers, the output force measured by the transducer is in Volts and we converted it into force units Newtons. To do this, each experiment was individually calibrated. After each experiment, monolayers were broken if they had not already failed. In these conditions, all of the force measured by the force transducer is due to the deflection of the soft wire, d_W, and it can be determined using the force-deflection equation for a simple cantilever beam.

$$F = k\ d_W, \tag{1}$$

where k is the stiffness of the wire defined as:

$$k = \frac{3EI}{L^3}. \tag{2}$$

E is the elastic modulus of the wire (previously determined in [19]), I its moment of inertia and L its length.

To determine the conversion between Volts and Newtons, for each experiment we collected 6 voltage, deflection pairs (V, d_W) and fitted them to a linear function. Using this procedure, we could determine the conversion factor α to convert Volts into Newtons:

$$\alpha = \frac{1}{V}\frac{3EI}{L^3}d_W. \tag{3}$$

In our mechanical characterisation of monolayers, we decided to approximate the tissue to a thin two-dimensional sheet and normalised the force F exerted on the monolayer to the average width of the monolayer before stretch w_0,

$$\frac{F}{w_0} = \frac{\alpha V}{w_0}, \tag{4}$$

where w_0 was sampled from three positions in the monolayers and computed as

$$w_0 = \frac{l_1 + 2l_2 + l_3}{4}, \tag{5}$$

where l_1 and l_3 correspond to the length of the monolayer on each of the sides where it contacts the rods and l_2 is the length at the middle point of the monolayer (**Fig.1 f**, inset).

All the tension measurements in this manuscript have been calculated using the initial width of the monolayer w_0 as defined in **eq.**5 unless otherwise specified. Generally, tension measurements were smoothed with a moving average sliding fixed-time window around the time point of interest (30 points for strain rates above 1% s^{-1}, 100 for 0.3% s^{-1} and 300 for 0.1% s^{-1}).

Strain energy measurements were determined by integrating the area of the tension-strain curves up to the rupture point.

All the analysis was implemented in MATLAB R2019a, MathWorks.

Pre-tension measurements

Epithelial monolayers are intrinsically under tension due to forces generated by myosin contractility in the cells [20], [21]. These intrinsic forces generate a deflection on the flexible arm of the device that corresponds to the pre-tension of the monolayer. This pre-tension was determined from two bright-field microscopy images, one acquired at the beginning of the experiment and the other at the end once the monolayer was broken. Both images were taken when no parts of the mechanical testing system contacted any of the rods of the device. A stack of these two images was generated and a region of 250×150 pxl^2 area was cropped around the flexible arm to measure its displacement, Δx, using a custom-made script in MATLAB. Using Hooke's law the pre-tension of the monolayers is:

$$\frac{F_0}{w_0} = -k\frac{\Delta x}{w_0}, \tag{6}$$

where k is given by **eq.**2.

Tension gradient measurements

To determine the tension gradient of monolayers, we first fitted a smoothing spline to the experimental tension-strain curves. We then computed the derivative of this curve before fitting it with a smoothing spline to reduce noise. These operations were implemented in MATLAB R2019a, MathWorks.

High magnification imaging devices

Devices used for confocal imaging to determine protein localisation as well as cell shape changes were similar to those described in [22]. Briefly, a glass capillary was bent into a U-shape using a small blow torch. One of the arms of the U-shaped capillary was cut at $\sim$ 5 mm from its base; in this arm, a nickel-titanium (nitinol) wire (Euroflex) was inserted to act as a hinge and covered

by another piece of a glass capillary. Glass coverslips (VWR) were affixed using UV-curing glue (Loctite Glassbond, 447 Henkel) to the extremities of the glass capillaries to act as a substrate for cells to grow on. For precise control when stretching the monolayers, another piece of glass capillary was glued onto the end of the flexible arm at an angle to allow continuous contact with the manipulator arm.

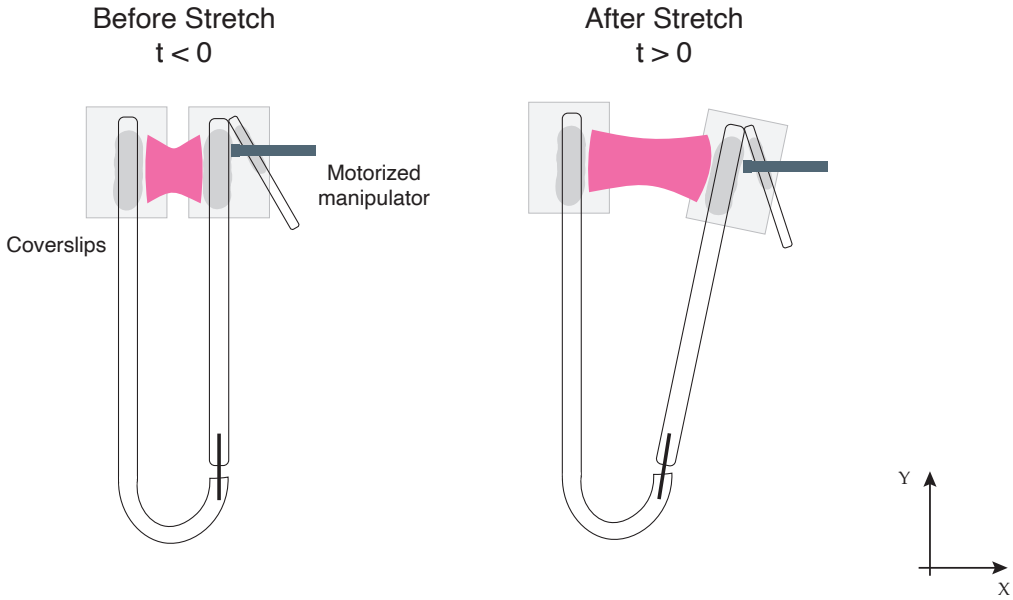

Figure 8: Example of a high magnification imaging stretching device. Shaded areas in dark gray depict the UV-glue used to affix the glass capillaries to the coverslips.

Confocal imaging of tissues and mechanical manipulation

Epithelial monolayers were imaged at room temperature in imaging medium. To visualize cell membranes, tissues were incubated for 10 min with CellMask membrane stain following the manufacturer protocol (Thermo Fisher Scientific). To visualize cell-shape changes by dye exclusion, AlexaFluor-647-conjugated dextran, 10,000 MW (Thermo Fisher Scientific) was added to the imaging medium to a final concentration of 20 µg mL^{-1}. Confocal images were acquired using a 60X Sil objective (UPLSAPO-S, numerical aperture 1.3, Olympus) mounted on an Olympus IX83 inverted microscope equipped with a scanning laser confocal head (Olympus FV-1200). Images consisted of a z-stack acquired at a spatial interval of 0.5 - 1µm. To generate time series, stacks were acquired every 50 s during stretching experiments and every 5 min in experiments in which monolayers were treated with calyculin. High magnification bright field images in **Fig. 1i** were taken using a 40X objective (Olympus, LUCPlanFL N) on an inverted Olympus IX71 microscope attached to a GS3-U3-60QS6M-C, Point Grey camera.

Immunohistochemistry assays

To visualise the organisation of the cytoskeleton and junctional proteins, we used immunostaining. For imaging of intermediate filaments, cells were fixed with a 1:1 mix of Methanol and acetone at -20 °C for 10 minutes. For all other proteins, cells were fixed in 4% paraformaldehyde diluted in DMEM without phenol red for 15 minutes. Cells were then washed three times with PBS to remove any fixative. Cells were permeabilised with 0.5% Triton 100X in PBS for 5 min at room temperature. After permeabilisation, cells were washed three times with PBS and blocked with 10% horse serum (HS) in PBS for 1h at room temperature changing the blocking buffer every 15 min. Next, cells were incubated with the primary antibodies for 2h at room temperature in a solution of 10% HS in PBS. After washing three times with PBS, the cells were incubated with Phalloidin 647 or 568 (Life technologies, 1:500) along with the alexa conjugated secondary antibodies for 1h at room temperature in a solution of 10% HS in PBS. Finally, cells were washed three times with PBS. The following primary antibodies were used: mouse anti-phospho-myosin light chain 2 (S19) (Cell Signaling 3675S, 1:100 dilution), mouse anti-E-cadherin (BD Biosciences 610181, 1:200 dilution), mouse anti-cytokeratin-18 (abcam ab668, 1:100 dilution), rabbit anti-alpha-catenin (Sigma Aldrich C-2081, 1:200), and rabbit anti-Desmoplakin (abcam ab71690, 1:100).

Drug treatments

To block Myosin contractility, blebbistatin (Sigma-Aldrich) was added at 50 µM concentration. To increase Myosin contractility, we inhibited phosphatases using calyculin A (Sigma-Aldrich) at 20 nM. To block actin polymerization, latrunculin B (Calbiochem) was used at 1 µM. DMSO was added in control monolayers accordingly. Drug treatments were added for 20 minutes before performing the ramps in deformation. To study ruptures caused by increases in internal contractility, calyculin was added at time 0 until full rupture of the monolayer. In immunostainings, drugs were added 15 minutes before fixation.

Measurement of junctional protein recruitment in response to strain

Fluorescence Intensity Measurements in XYZ-t images

Z-stacks were acquired at 1 minute intervals, starting 5 minutes before stretch, and continuing for 30 - 80 minutes. The planes in which we measured the fluorescent intensity were selected by comparing a maximum intensity projection image (MIP) with all the planes at each time-point. This was done using 2D cross-correlation. Alignment between the last time point before stretch and the first one after stretch was done using 2D cross-correlation to ensure similar fields of view were compared. After this, a movie with the optimum z-planes is created and saved for further processing. Segmentation of cell membranes was carried out with Packing Analyzer to generate a mask containing all of the cell junctions. These masks were then processed in MATLAB. A second registration is performed to ensure the masks overlap correctly with each of the images of the movie. Finally, the intensity of each pixel within the mask was extracted from the aligned movies and averaged to output the mean fluorescence in the region of interest at each time point. All processing after segmentation was performed in MATLAB (as shown in **Fig. 10**)

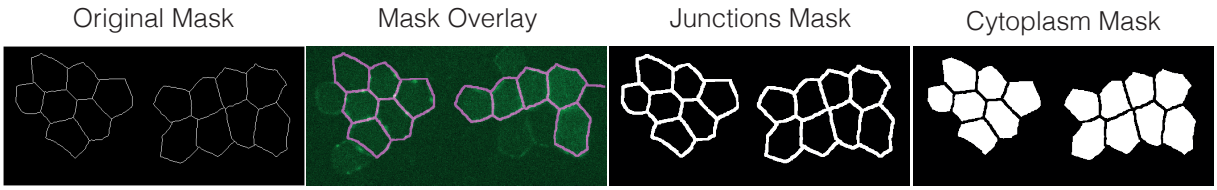

Figure 9: Processing of segmentation masks to perform fluorescence intensity measurements in either the junctions or the cytoplasm.

Fluorescence Intensity Measurements at individual junctions in profiles of E-cadherin-GFP monolayers

XYZ stacks or XZ profile views of E-cadherin-GFP monolayers were acquired every 50 seconds to evaluate changes to junction morphology in response to stretch. Segmentation was carried out with a machine learning plugin in Fiji [54], Weka segmentation. First, several planes were used to manually train the segmentation plugin which was then applied to the whole movie. The masks obtained from Fiji were then processed in MATLAB (as shown in **Fig. 10**). First, bright objects from the binary image were selected using a threshold based on a fluorescent intensity histogram. Then, bounding boxes were used to find the previously selected bright objects. Junctions were afterwards chosen by applying length, width, and area thresholds to the bounding boxes. Normally, we ensured that the width of the bounding box was smaller than its height, and bounding boxes with an area smaller than 50 - 80 pxl^2 were discarded. Final masks were overlayed on the original image to confirm a good correlation between both images. Fluorescence intensity was then measured in each junction over time.

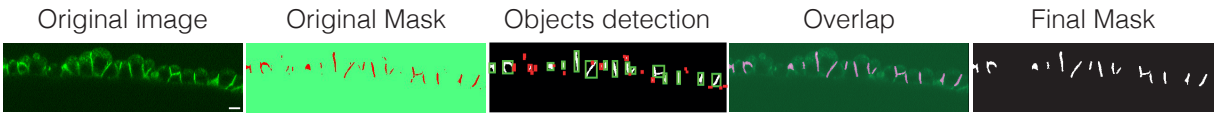

Figure 10: Processing of microscopy images of E-cadherin-GFP monolayers.

Statistical Analysis

Statistical analyses were done using MATLAB R2019a (Mathworks, Natick, MA, USA).
Box plots show the median of the distributions with a central bar, the 25th (first quartile, Q1) and 75th percentiles (third quartile, Q3) are represented by the bounding boxes and the most extreme data points without the outliers are represented by the whiskers. Outliers were defined as being either larger than $Q3 + 1.5IQR$ or smaller than $Q1 - 1.5IQR$, with $IQR = Q3 - Q1$. They appear outside the range of the whiskers and are represented by the symbol '+' in red. In all box plots, statistically significant difference are indicated by: ns non significant, P $>$ 0.05, *P $<$ 0.05, **P $<$ 0.01, ***P $<$ 0.001, ****P $<$ 0.0001. Statistical significances were computed using a Kolmogorov-Smirnov-test. The number of monolayers (unless otherwise specified in the legend) examined in each condition is indicated above each box plot.

Computational model

Molecular bond dynamics model

The rupture of a junction is modelled from the dynamics of a population of N links, each having a slip bond behaviour, i.e. a rate of binding k_{on} that is assumed to be constant, and a rate of unbinding k_{off} that is force dependent, $k_{off} = k_{off,0} \exp(f/f_0)$, where f is the force on the link [55]. In this implementation, the force on the junction F is distributed evenly over all the bound links. If, at a certain time, there is a number n_b of bound links, the force per link is $f = F/n_b$.

The system is first initialised with a random distribution of states across the N links, with a probability to be bound given by $k_{on}/k_{off,0}$. The overall force over time $F(t)$ follows precalculated curves based on the selected rheology. It is here assumed that stress is homogeneously distributed in all junctions, and therefore that the junction force F is simply proportional to the tissue tension Γ.

To simulate the evolution of the population, a small timestep dt and discrete probabilities that junctions change state are defined at each time point based on the current force. The state of the system then evolves in a stochastic manner based on these probabilities. The model runs until the end time point is reached, or until all links are unbound, which corresponds to the rupture time t^*. The model has four parameters. We fixed two parameters, the number of linkers $N = 100$, and set the ratio $k_{on}/k_{off,0} = 10$. The values of the force f_0 and k_{on} were then varied to best match the experimental data once combined with the non-linear visco-elastic model presented below. The parameter values are presented in **Table S7**.

Linear and non-linear rheology

In the experiments and the model, the strain is controlled, and the mechanical tension $\Gamma(t)$ of the epithelium is calculated using a rheological model. For a given strain rate $\dot{\varepsilon}$, the strain function is given by $\varepsilon(t < 0) = 0$ and $\varepsilon(t \geq 0) = \dot{\varepsilon}t$. For the linear spring model, the tension is proportional to the strain: $\Gamma = k_a\varepsilon$. For the fractional model, the calculation of the tension follows the method presented in [42], calculated using the software package RHEOS [56].

The non-linear spring model corresponds to a monotonically increasing relationship between Γ and ε. To define this relationship, we assume that strain-stiffening arises from the progressive recruitment of intermediate filaments as the strain is increased (in addition to the linear term defined in the previous paragraph). The strains at which fibers are recruited are modelled as a compact triangular distribution $p_s(\varepsilon)$ over a domain [0, 2.2], with a maximum in the middle (**Fig. S9d**). These bounds are based on the range of strains for which strain stiffening is observed in the experiments at high strain rates. The tension in the tissue is then calculated by superposition:

$$\Gamma(\varepsilon) = k \int_0^{\varepsilon} p_s(\varepsilon') \left(\varepsilon - \varepsilon'\right) d\varepsilon' + k_a\varepsilon. \tag{7}$$

The non-linear viscoelastic model builds on the previous description, but assuming that once loaded, each filament behaves in a Maxwell-like manner. For a single Maxwell model with a spring k and

a dashpot η, the response to the ramp in strain with rate $\dot{\varepsilon}$ is given by $\eta\dot{\varepsilon}(1 - \exp(-t/\tau))$ with $\tau = \eta/k$. The full response is again obtained by superposition:

$$\Gamma(t) = \eta\dot{\varepsilon} \int_0^{\dot{\varepsilon}t} p_s(\varepsilon') \left(1 - \exp\left(-\frac{\dot{\varepsilon}t - \varepsilon'}{\dot{\varepsilon}\tau}\right)\right) d\varepsilon' + k_a\dot{\varepsilon}t. \tag{8}$$

The distribution p_s is adjusted to mimic the high strain rate limit, identical to the non-linear spring model (**Fig. S 9d**). The extra parameter η (or equivalently τ) is adjusted to account for the observed timescale associated with the shear stiffening behaviour. The parameter values used in the different rheological models are presented in table **Table S8**.